Superior visible light-mediated catalytic activity of a novel N-doped, Fe_3O_4-incorporating MgO nanosheet in presence of PMS: Imidacloprid degradation and implications on simultaneous bacterial inactivation

Somaye Akbari [a], Gholamreza Moussavi [a,*], Jeremie Decker [b,c], Maria Luisa Marin [d], Francisco Bosca [d], Stefanos Giannakis [c,*]

[a] Department of Environmental Health Engineering, Faculty of Medical Sciences, Tarbiat Modares University, Tehran, Iran
[b] École Polytechnique Fédérale de Lausanne (EPFL), School of Architecture, Civil and Environmental Engineering (ENAC), Environmental Engineering Institute (IIE), GR-LUD, Station 6, CH-1015 Lausanne, Switzerland
[c] Universidad Politécnica de Madrid, E.T.S. Ingenieros de Caminos, Canales y Puertos, Departamento de Ingeniería Civil: Hidráulica, Energía y Medio Ambiente, Unidad docente Ingeniería Sanitaria, c/ Profesor Aranguren, s/n, ES-28040 Madrid, Spain
[d] Instituto de Tecnología Química, Universitat Politècnica de València-Consejo Superior de Investigaciones Científicas, Avenida de los Naranjos s/n, 46022 Valencia, Spain

ARTICLE INFO

ABSTRACT

Impressive Imidacloprid (IMD) degradation and bacterial inactivation were attained through the photocatalytic activation of peroxymonosulfate (PMS) via a novel, N-doped $MgO@Fe_3O_4$, under visible light. After complete characterization (XPS, XRD, FT-IR, FE-SEM, EDX, HRTEM, DRS, BET, VSM, and EIS), using [PMS]=75 mg/L, [N-$MgO@Fe_3O_4$]=150 mg/L at pH=5.6, around 95% of 10 mg/L IMD was degraded within 60 min; highly synergic interactions between the various catalytic routes were revealed. Extensive scavenger tests and EPR studies revealed that $SO_4^{\bullet-}$, $HO^{\bullet}$, and $^1O_2$ are generated and play a key role in IMD degradation. Tap water experiments proceeded unhindered, and only the presence of high HCO_3^- and PO_4^{3-} concentration resulted in a decrease in the IMD degradation efficiency, while negligible leaching, magnetization, notable separation, and reusability properties were well-preserved for six repetitive cycles. Finally, *E. coli* disinfection was achieved before IMD degradation, possibly affected by its transformation byproducts. The overall efficacy of N-$MgO@Fe_3O_4$ indicated the potential for implementation in contaminated waters.

1. Introduction

Over the last decades, urbanization and the trend of increasing population growth caused to enhance the need for intensified crop production. The most important challenges for governments are to secure adequate amounts of food, which increased agronomic crops in the world. To safely cultivate products against pests, insects, and herbs, different types of pesticides such as organochlorine, organophosphorus, carbamates, and pyrethroids are applied by farmers [1]. Consequently, along with agrochemical substance consumption and often abuse, severe pollution of water resources through the run-offs and agro-industrial wastewater has occurred. The main issue about pesticides as emerging pollutants is their unwanted accumulation in human tissues via the food chain, which causes humans to exposure to a high concentration of toxins [1,2].

Imidacloprid (IMD) is a neonicotinoid insecticide, which is broadly applied to protect crops against herbivorous pests, for instance, greenflies, aphids, weevils, and other harmful insects. It is also used as a seed dressing agent to prevent the transmission of plant pathogens, and for this reason, has attracted growers' attention; for instance, China's IMD consumption reached 11.4 thousand tons in 2011 [3,4]. Because of its worldwide use, the residues of IMD in water supplies have been reported to range from 0.0021 to 3.623 ng/L. Due to its high hydro-solubility (0.51 g/L), stability (190 d), and mobility, IMD induces water quality problems around the globe countries. Additionally, IMD has demonstrated a toxic character in human health and non-targeted animal species, such as bee colonies. Hence, it is utterly important to develop an effective method for treating contaminated water with this kind of

pesticide [3,5–7].

In addition, microbial pollution is another critical aspect of water quality; apart from the chemical contaminants of emerging concern (CECs), the presence of microorganisms in effluents must be dealt simultaneously with the presence of CECs. Chlorination has been the method of choice conventionally used for water disinfection. Despite its unique merits, including the residual activity in the treated water for preventing regrowth and post-treatment growth of bacteria, chlorine reacts with the organic matter resulting in forming toxic by-products [8]. Therefore, Advanced Oxidation Processes (AOPs), a family of methods capable of simultaneously eliminating CECs and microbial contamination, are of great importance and thus have attracted the interest of researchers in the field.

Among the AOPs tested for the degradation of pesticides [9], the photocatalytic methods are an interesting technological option that has been applied in the degradation of various recalcitrant organic compounds. Photocatalytic oxidation driven by visible light is a growingly chosen variant among the other light sources, like UV radiation, resulting from its economic character and safety energy point [10]. As the light reaches the reaction solution, the electron in the catalysts is excited and moves from the valance band to the conduction band. Consequently, active species such as electron-hole pairs and other reactive intermediates are generated, and degradation of pollutants takes place by both direct and indirect redox reactions [11–13]. Semiconductor materials including TiO_2, ZnO, BiO_2, Al_2O_3, Cu_2O, some metal oxides, and a few nonmetals have been reported in photocatalytic oxidation applications for accelerating contaminant degradation due to their optical characteristic and suitable potential for light exploitation [14–18]. Among the various metal oxides already tested, magnesium oxide (MgO) has gained broad attention due to a series of advantages, such as its accessibility, cost-effectiveness, chemical balance, harmless nature, and high specific surface area [19,20].

Considerably, in several studies, MgO has been successfully employed in photocatalysis (alone), enhancing ozonation, adsorption, and biological processes, to remove organic and inorganic compounds [21–24]. However, the photocatalytic activity of MgO under visible light is limited by intrinsic properties, such as its wide bandgap, which results in decreased photogenerated electron-hole pair induction [21]. Accordingly, multiple attempts have been dedicated to minimizing the energy gap and improving the photo-efficiency. Doping of semiconductors with nonmetals like C, P, F, and S might be an attractive alternative to both shifting in absorption edge toward the visible light range and decreasing the electron-hole recombination rate and providing efficiency to catalyst activation under visible light [25–27]. Under this scope, nitrogen is an interesting dopant for alteration of the electronic structure of materials, inducing favorable conditions above the valence band by promoting the number of active sites and oxygen vacancies [28]. In addition, nitrogen species indicated the best result for modification of TiO_2 and ZnO due to their minimum energy for dissociation, stability, easy replacement with oxygen, and narrowing bandgap [29,30].

Besides bandgap engineering, photocatalysis is often presented with an additional challenge, i.e., secondary catalytic pollution. The recovery of nanocomposites from the reaction mixture is a serious problem resulting from their small size. Different methods were reported for solving this problem. Recently, magnetic catalysts have attracted interest in catalytic applications, inducing easy separation, and high reusability [31]. In many studies, compositing magnetite (Fe_3O_4) with a prepared catalyst can be an excellent suggestion for this problem [32,33]. However, the modification of a catalyst can enhance its photo-activity, but sometimes it can result in fast recombination of carrier species or a shift in the photo-produced reactive intermediates generated, causing a decrease in its efficacy. To overcome this drawback, an electron acceptor for instance oxygen or peroxymonosulfate (PMS) can be applied with the aim to exploit the ample electron excitation and produce further oxidative species [34].

In this context, although the superoxide radical anion of oxygen ($O_2^{\bullet-}$) generated from molecular oxygen can lead to the removal of pollutants and bacterial inactivation, sulfate radicals and hydroxyl radicals generated from PMS and/or the valence band vacancies are some more of the possible photo-produced reactive species. Sulfate radical-based AOPs (SR-AOPs) including the sulfate ($SO_4^{\bullet-}$) and hydroxyl ($HO^{\bullet}$) radicals have received wide attention in environmental applications [11,19]. These radicals are very important reactive species in degradation reactions [7,35,36]. $SO_4^{\bullet-}$ is generated mainly through activation of peroxymonosulfate (PMS) by UV radiation, heating, and reaction with transition metals such as Ni(II), Mn(IV), Fe(II), Ce(III), and Ag(I) has a long lifetime (30–40 µs) and oxidation potential between 2.5 and 3.1 V [37]. In the case of $HO^{\bullet}$, its oxidation potential is between 1.8 and 2.7 V vs. NHE and can also be generated from PMS (more likely at neutral/basic pH values), or the occurring photocatalytic processes by using semiconductors such as TiO_2, ZnO, or WO_3 [38].

Taking into account the above considerations, this work was aimed at developing a visible-light assisted photocatalytic PMS activation process with a novel, nitrogen-doped, magnetite-containing MgO nanocatalyst. We modified MgO through one-step doping by nitrogen, with a new approach into facile preparation of catalysts for PMS activation and photocatalytic reactions, followed by anchoring functionalized Fe_3O_4 nanoparticles. The novel catalyst was fully characterized by a wide array series of tests, for its chemical, functional and mechanical properties. Using this heterogeneous system, the photocatalytic degradation of IMD and inactivation of bacteria by the simultaneous generation of oxidative species were scrutinized. Accordingly, several experimental factors including pH, catalyst and PMS concentration, the effect of water anions, and catalyst stability over reuse were carried out in this work. Besides IMD removal, the bactericidal efficacy of the photocatalytic process was also assessed, in competitive IMD degradation/disinfection tests. Moreover, via the study of mineralization, dichlorination, denitrogenation, and intermediate degradation products generation, combined with ample scavenger study tests and EPR analysis, the underlying photo-catalytic mechanisms, and the pathway to degradation of IMD are proposed.

2. Materials and methods

2.1. Chemicals and reagents

All the chemicals and reagents used in the present study were of analytical grade and used as received. In this work, all solutions were prepared with deionized water.

2.2. Preparation of Fe_3O_4 nanoparticles

The preparation of the magnetite nanoparticles was performed according to a previously published method [39]. Briefly, 1.36 g of $FeCl_3.6\,H_2O$, 2.4 g of sodium acetate, and 0.4 g of $Na_3C_6H_5O_7.2\,H_2O$ were dissolved in 40 mL ethylene glycol. The solution was stirred for 1.5 h, then transferred to a Teflon-lined stainless-steel autoclave and heated at 200 °C for 15 h. After cooling to room temperature, the product was collected by an external magnet, rinsed with deionized water and ethanol several times, and dried in an oven (80 °C for 5 h).

2.3. Synthesis of N-MgO@Fe_3O_4

N-MgO was synthesized based on the sol-gel method. Briefly, 2.0 g of $Mg(C_2H_3O_2)_2$ was dissolved in 100 mL of distilled water and stirred for 30 min. Then, an equal ratio of urea to magnesium was added to the above solution, and stirring was continued for 2 h. Sufficient volume of ammonia solution was added to the above mixture and was stirred for 18 h to form the gel. The prepared gel was centrifuged (5000 rpm) and washed with water/ethanol several times. The washed gel was dried in

an oven (110 °C for 2 h). Finally, the as-prepared product was heated and calcined at 500 °C for 2 h at a heating rate of 4 °C min^{-1}. The same procedure was used for synthesizing plain MgO, but without using urea.

To prepare the Fe$_3$O$_4$ anchored to the MgO or N-MgO, 0.02 g of as-made Fe$_3$O$_4$ were dispersed in 10 mL of methanol, then 0.66 g of PVP and 20 mL of DMF were added to the solution, and the mixture was sonicated for 6 h. Afterward, the as-prepared Fe$_3$O$_4$ nanoparticles were separated from the reaction media by a magnet and then dried in an oven (at 80 °C for 5 h). Following, 0.02 g of as-prepared Fe$_3$O$_4$ and 0.1 g of MgO or N-MgO materials were separately dispersed in 20 mL distilled water. The ratio of MgO or N-MgO to Fe$_3$O$_4$ was selected based on the published literature [40,41]. The two suspensions were mixed for 10 min and were then sonicated for 5 h. Finally, the product was collected by an external magnet, rinsed with deionized water several times, and dried in an oven at 80 °C for 8 h.

2.4. Material characterization methods

The crystalline phase of the prepared catalyst was detected based on the X-ray diffraction (XRD, KEFA) template in the 2θ scanning range from 10 to 80° and Cu as anode material with Kα1 of 1.5406. The chemical bonds were identified by a Fourier transform infrared spectroscopy (FTIR, Perkin Elmer) in the frequency range of 400–4000 cm^{-1}. The surface structure and elemental distribution of the as-prepared catalyst were determined by field emission scanning electron microscopy (FESEM, XL30 Philips) coupled with Energy-dispersive X-ray spectroscopy (EDAX). The actual size of N-MgO@Fe$_3$O$_4$ was obtained by transmission electron microscopy (TEM) using Philips CM30. The specific surface area was characterized by Brunauer-Emmett-Teller (BET, Belsorp mini II) in the condition of nitrogen adsorption/desorption at 77 k. To measure, the magnetic properties of the catalyst, a vibrating sample magnetometer (VSM, LBKFB) was used. The energy bandgap and photoelectronic properties were evaluated by differential reflectance spectroscopy (DRS, Shimadzu), respectively. X-ray photoelectron spectroscopy (XPS) was performed using an Escalab 250 apparatus. Inductively coupled plasma (ICP, Varian) analysis was used to measure the concentration of the residual metals. Electrochemical impedance spectroscopy (EIS) analysis was carried out by Potentiostat/ Galvanostat (IVIUM Vertex) with the open circuit potential using glassy carbon as working electrode, Calomel as reference electrode frequency, Na$_2$SO$_4$ (0.3 M) solution, the frequency of 0.01 Hz–10^6 Hz, and the amplitude of 0.01 V. Finally, the identification of intermediates during the IMD photodegradation was conducted by Liquid Chromatography-Mass Spectrometry (LC/MS) analysis (2695 HPLC-Micromass Quattro micro API, Waters Alliance).

2.5. Photocatalytic experiments and analytical methods

The photocatalytic performance of N-MgO@Fe$_3$O$_4$ for IMD degradation was conducted in a batch-quartz photoreactor (diameter of 10 cm and volume of 50 mL). In the photo-based processes, four 6-W Xenon lamps were used to irradiate the reactor from the top. The emission spectrum of the lamps shown in Fig. S1 indicates that they emitted photons with the dominant wavelengths of 450 nm with a light intensity of 43 mW/cm^2 at 555 nm with a light intensity of 19 mW/cm^2. All experiments were conducted at room temperature and atmospheric pressure. In addition, all catalytic experiments were conducted in triplicates and the average results were reported. The standard deviation was predominantly below 5% in most of the experiments, showing the repeatability of the results; to prevent messing up the figures, the error bars were not shown (included only in cases with higher SD).

Three main types of reactions were run with IMD as a target: photocatalysis, PMS catalytic activation, and PMS-assisted photocatalysis:

A. In the photocatalytic experiments, a predetermined amount of catalyst was dispersed into 15 mL of IMD solution (10 mg/L) with a

target pH in the reactor and the stirrer and the lamps were immediately switched on. After the specified reaction time was up, the lamps and the stirrer were turned-off and 5 mL of sample was filtered through a syringe filter (0.2-μm pore size). The residual concentrations of IMD and total organic carbon (TOC) were then determined in the filtrate.

B. In the PMS catalytic activation experiments, the same procedure as the photocatalytic experiments were undertaken except that a given amount of PMS was added to IMD solution with (no irradiation).

C. In the PMS-assisted photocatalytic experiments, the same procedure of photocatalytic experiments along with adding a given amount of PMS to the solution was employed. It should be mentioned that the adsorption (no irradiation and PMS addition) and visible light activation (VL/PMS) processes were also conducted as the control measures.

The concentration of IMD was measured by a high-performance chromatography (HPLC, Eclipse Plus C18 column; 3.5 μm, 4.6 × 100 mm, Agilent) with a UV detector at 275 nm. The mobile phase was a mixture of water and acetonitrile (1:1 vol%) injected at a flow rate of 1 mL/min. The concentration of TOC was determined using Shimadzu TOC Analyzer (TOC-L CSH/CSN). The performance of the developed catalytic process was then evaluated based on IMD and TOC removal efficiencies calculated using the following equation:

$$\text{Removal } efficiency(\%) = \left(1 - \frac{C_t}{C_0}\right) \times 100 \quad (1)$$

in which, C$_0$ and C$_t$ are the initial and final concentrations of IMD or TOC. All the experiments were conducted at least in duplicate, and the mean of the results is reported.

The main intermediates formed during the degradation of IMD in the PMS-assisted photocatalytic process as the best-performed process among the tested ones operated under optimum experimental conditions were identified using liquid-chromatography-mass spectroscopy (LC-MS, 2010 A/Shimadzu) coupled with an Eclipse Atlantis T3, C18 column (2.1 × 100 mm, 3.0 μm particle size) at ambient temperature. The mobile phase of this analysis consisted of acetonitrile (containing 0.1% formic acid], and water (containing 0.1% formic acid), with an injected flow rate of 0.2 mL/min, and a sample volume of 5 μL. In addition, the following conditions were selected for the Mass spectrophotometer: gas nebulizer: nitrogen (N$_2$), capillary volt: 4.0 kV, Cone volt: 30 V, flow gas: 200 L/h, while source and desolation temperatures were 120 °C and 300 °C, respectively. The spectrophotometer scanning was collected for the 50–500 *m/z* range.

2.6. Electron paramagnetic resonance (EPR) experiments

A Bruker EMX 10/12 EPR spectrometer and the following experimental conditions were employed for the EPR measurements: microwave power: 20 mW; modulation amplitude: 1.0 G; and modulation frequency: 100 kHz. Samples were placed in a Wildman Suprasil/ aqueous quartz ware flat cell (volume of 150 μL, 60 mm in length) and were irradiated simultaneously to acquire the EPR signal with a Xe lamp (0.12 W/cm^2). The probes TEMP (2,2,6,6-tetramethylpiperidine) and DMPO (5,5-dimethyl-1-pyrroline-N-oxide) were from Sigma-Aldrich and TCI Europe, respectively, and used as received. D$_2$O was employed as a solvent for the EPR experiments conducted in the presence of TEMP.

Detection of ^{1}O$_2$ was carried out as follows: TEMP (1.2 mM) was added to an aerated mixture of N-MgO@Fe$_3$O$_4$ (150 mg/L) and PMS (75 mg/L) in D$_2$O at pH ca. 6. Afterward, the sample was vortexed for 1 min and submitted to EPR under simultaneous irradiation using a 380 nm cut-off filter. Control samples of TEMP (1.2 mM) and only N-MgO@Fe$_3$O$_4$ (150 mg/L) or PMS (75 mg/L) in aerated D$_2$O were also analyzed.

EPR experiments for the detection of HO$^{\bullet}$/ SO$_4^{\bullet-}$ were performed as follows: DMPO (10 mM) was added to a de-aerated aqueous mixture of N-MgO@Fe$_3$O$_4$ (150 mg/L) and PMS (75 mg/L) at pH ca. 6. Then, the sample was vortexed for 1 min and submitted to EPR under simultaneous irradiation using a 435 nm cut-off filter. EPR measurements in the absence of light acted as a reference.

For the detection of O$_2^{\bullet-}$, DMPO (10 mM) was added to an aerated aqueous mixture of N-MgO@Fe$_3$O$_4$ (150 mg/L) at pH ca. 6, in the absence of PMS. Then, the sample was vortexed for 1 min and submitted to EPR under simultaneous irradiation using a 320 nm cut-off filter. EPR measurements were also carried out in aqueous ethanol (1:4, v:v) to eliminate the interference of DMPO-OH.

2.7. Disinfection experiments: bacterial methods and protocols

The bacterial targets used in this study are *Escherichia coli* and *Enterococcus* sp. wild-type strains, supplied by DSMZ Germany (Strain No. 498) and a natural isolate from urban secondary effluent via selection by Slanetz-Bartley selective Agar, respectively. The assessment of the photocatalytic efficacy using the specific two model microorganisms provides a trustworthy estimation for naturally occurring bacterial gram-negative and gram-positive pathogens in nature and or wastewater effluents. The cultivation method has been previously published [42, 43].

For the enumeration of microorganisms, 1 mL of sample was taken from the experimental matrix and spread-plated in 9-cm Petri dishes with Plate Count Agar (PCA, Sigma-Aldrich) when targeting *E. coli* or Slanetz-Bartley Agar (SBA, Panreac) when experimenting with *Enterococcus sp.*, respectively. Dispersion was performed by the standard spread plate method, followed by incubation for 24 or 48 h at 37 °C before the manual enumeration of *E. coli* and *Enterococcus sp*. All tests were performed at least twice (biological replicates), in duplicate series (statistical replicates), and by enumerating at least two consecutive aliquots (technical replicates). The graphed values show the average of the different tests, and the vertical bars indicate the standard deviation from the mean value.

3. Results and discussion

3.1. Characterization of N-MgO@Fe₃O₄ nanoparticles

The crystallographic structure of bare MgO, N-MgO, and N-MgO@-Fe$_3$O$_4$ catalysts is evaluated in Fig. 1 by XRD analysis. According to Fig. 1a, all diffraction peaks positioned at 36.9, 42.9, 62.3, 74.7, and 78.6 for sample "MgO" show the pure MgO planes 111, 002, 022, 113, and 222, respectively (Reference card code: 98–002–2099). As shown in the N-MgO plane, doping N atom has not changed the crystal phase of MgO. Moreover, the intensity and sharp peaks in the N-MgO plane could be attributed to improving its crystallinity in comparison with plain MgO. Regarding reference card code 98–006–1937 for Fe$_3$O$_4$, the diffraction peaks at 2 thetas of 30.2, 35.7, and 57.3 degrees in the XRD pattern of the N-MgO@Fe$_3$O$_4$ and N-MgO@Fe$_3$O$_4$ materials were related to 022, 113, and 115 planes of Fe$_3$O$_4$, respectively, which proved the presence of cubic structure of Fe$_3$O$_4$ in the final, as-prepared materials [39]. Therefore, observing the main diffraction peak of MgO (at 42.9 degrees) and of Fe$_3$O$_4$ (at 35.7 degrees) shows that the composite was well-prepared, and that compositing N-MgO with Fe$_3$O$_4$ did not change the crystal phase of MgO, and that the main characteristic peaks of MgO were observed in the N-MgO@Fe$_3$O$_4$ composite.

The FTIR spectra of the as-made N-MgO, MgO@Fe$_3$O$_4$, and N-MgO@Fe$_3$O$_4$ materials are presented in Fig. 1b. A broad peak at about 1480 cm^{-1} and moderate peaks at 3464 cm^{-1} and 3530 cm^{-1} are related to strong C-N and N-H bonds, respectively, which are formed by amine group deformity. It should be noted the sharp absorption peak at about 3600 cm^{-1} is associated with the stretching vibration of -OH bonds from hydroxyl groups on the surface and the H$_2$O molecules. This result also demonstrated the successful formation of Fe/Mg-O according to the wideband in the range 400–1000 cm^{-1}. The other absorption bands at 1677 cm^{-1} (for N-MgO), 2351 cm^{-1} (for N-MgO@Fe$_3$O$_4$), and 2960 cm^{-1} are associated with the C-O and C-H functional groups, respectively [44,45].

The surface morphology of the as-prepared N-MgO@Fe$_3$O$_4$ nanocomposite by FESEM images is presented in Fig. 1c. As it can be seen, the N-MgO@Fe$_3$O$_4$ nanocomposite had a regular structure with nanosheet
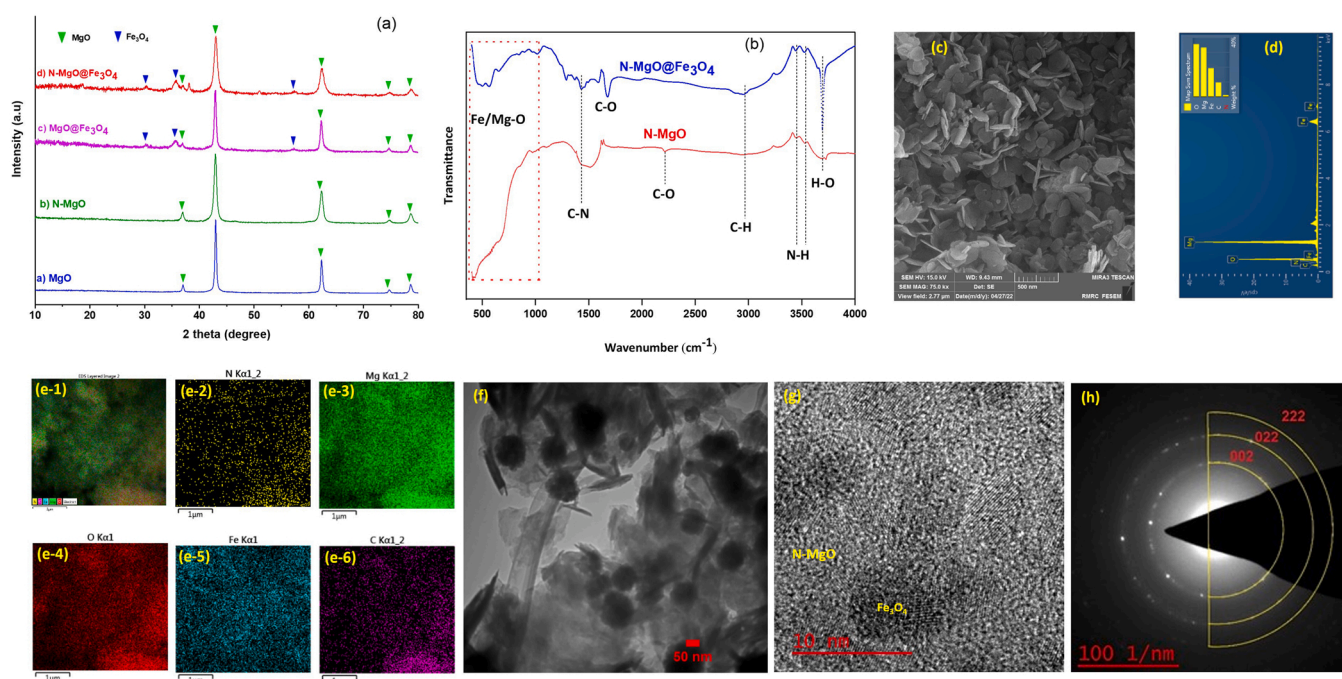

Fig. 1. XRD images of pure MgO, N-MgO, and N-MgO@Fe₃O₄ (a), FTIR patterns of as-prepared nanoparticles (b), FESEM images of N-MgO@Fe₃O₄ (c), EDX analysis of N-MgO@Fe₃O₄ (d), Elemental mapping of N-MgO@Fe₃O₄ (e), and TEM (f), HRTEM (g) and SAED (h) images of N-MgO@Fe₃O₄. (Fig. S2 depicts the TEM of MgO@Fe₃O₄).

morphology. To identify the elemental percentages in the as-made N-$MgO@Fe_3O_4$ nanocomposite structure, the EDX analysis was applied in conjunction with an SEM image: based on the EDX analysis shown in Fig. 1d, the co-existence of Mg, O, Fe, C, and N elements on the N-$MgO@Fe_3O_4$ was identified. The presence of these elements on the

surface of the N-$MgO@Fe_3O_4$ nanocomposite was confirmed by the SEM elemental mapping analysis of the powder (Fig. 1e). The element of carbon identified in the EDX/mapping elemental analysis comes from the linker used for composing N-MgO particles with Fe_3O_4 particles.

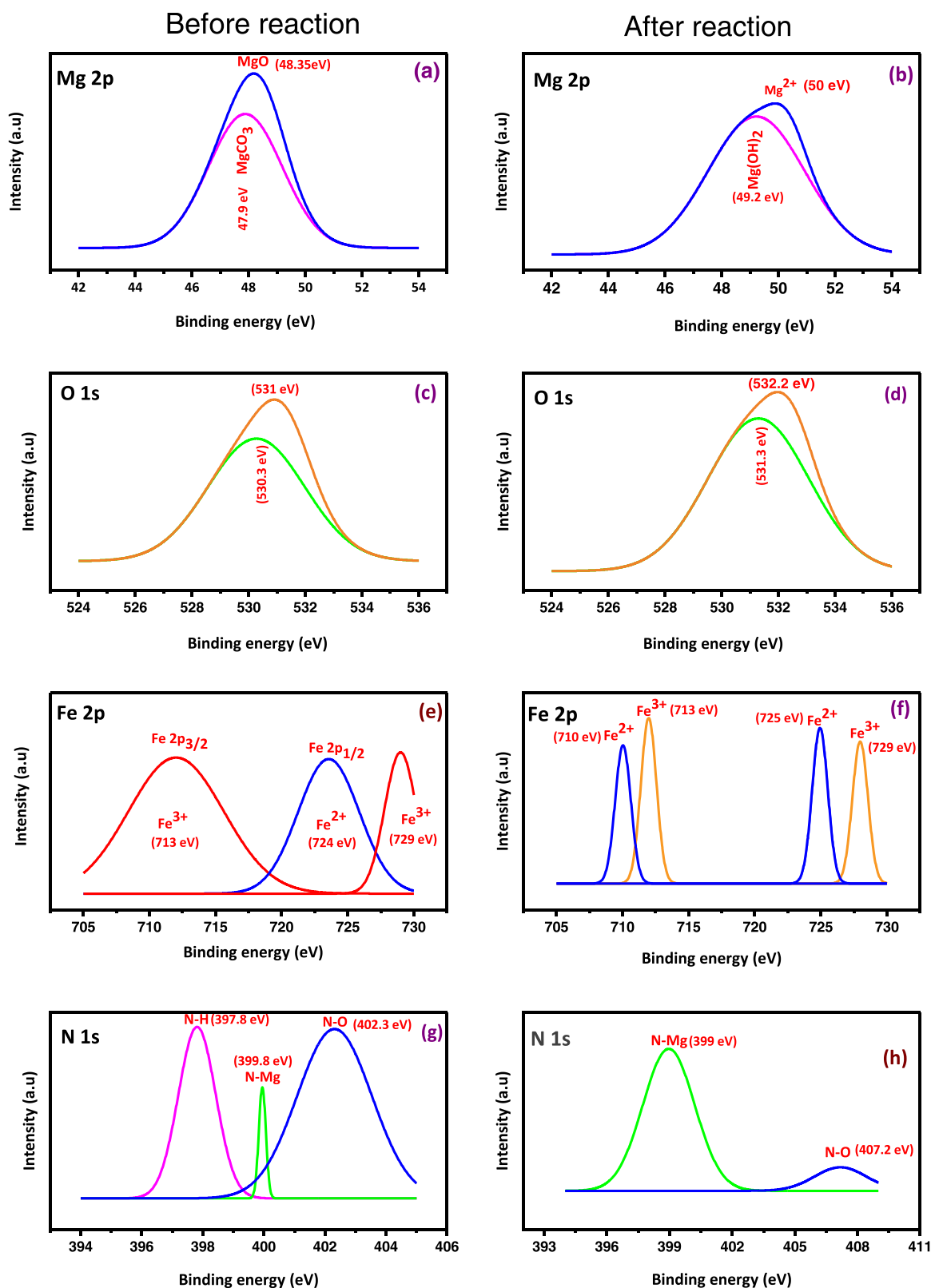To further examine the morphology and dispersion of the

Fig. 2. The deconvoluted high-resolution XPS spectra of N-$MgO@Fe_3O_4$ before (left column) and after the reaction (right column).

synthesized nanoparticles, the TEM analysis was conducted (Fig. 1f), and the HRTEM image is shown in Fig. 1g. According to the TEM image (Fig. 1f), the N-MgO has nanosheet morphology, and Fe_3O_4 nanoparticles were dispersed in spherical and regular shapes as black spots on the N-MgO nanosheets. Accordingly, the N-MgO nanosheets were well-decorated with spherical Fe_3O_4 particles. The presence of the spherical

Fe_3O_4 particles on the N-MgO nanosheets was reconfirmed by observing the lattice fringes in the HRTEM images of the composite shown in Fig. 1g. The spots and loops observed in the selected area electron diffraction (SAED) (Fig. 1h) indicate the polycrystalline structure of the as-made material. Based on the SAED image shown in Fig. 1h, the MgO planes of (002), (022), and (222) were present in the composite.
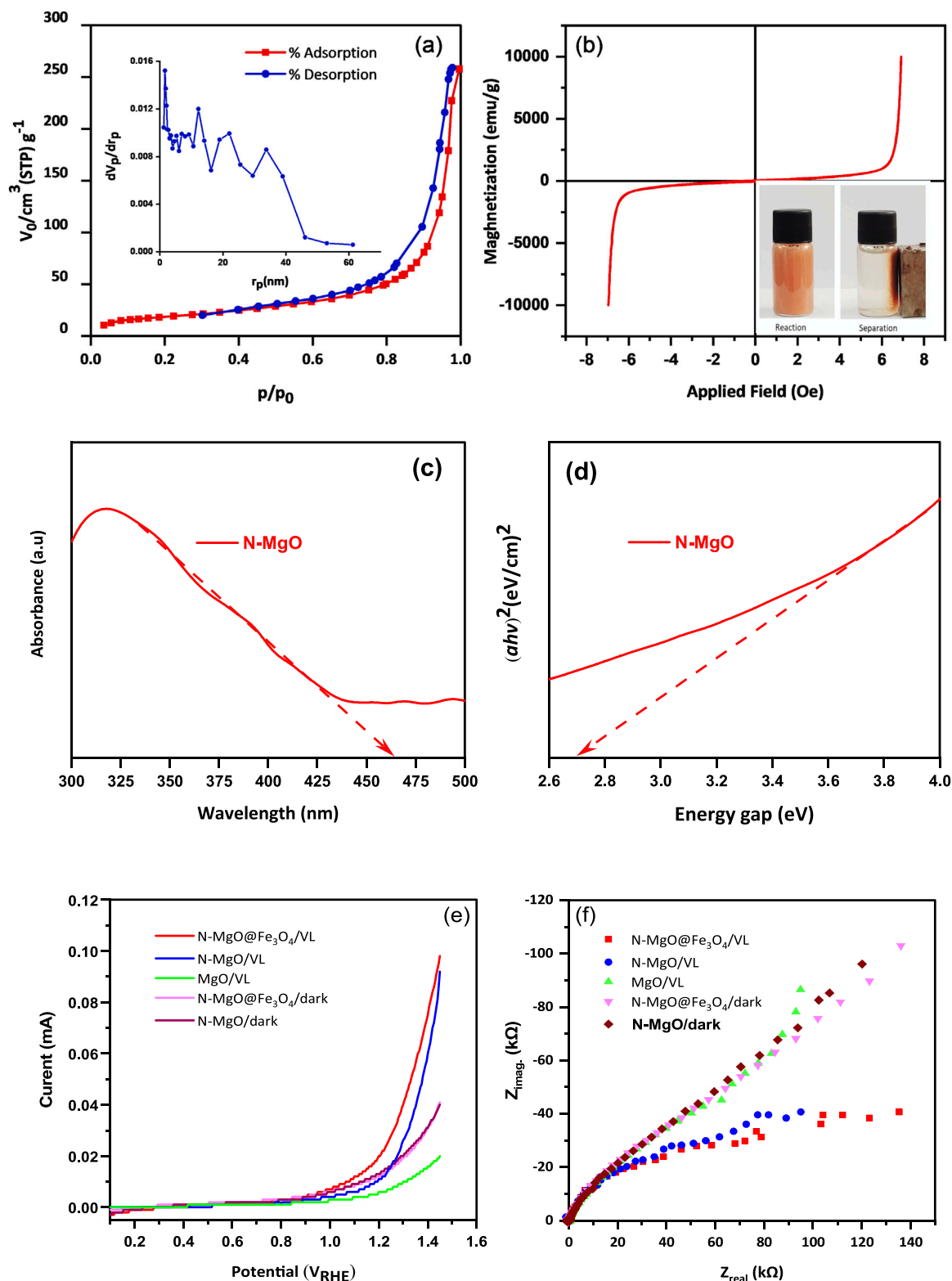
Fig. 3. BET analysis of the as-synthesized N-MgO@Fe₃O₄ and its BJH plot (inset) (a), Magnetic hysteresis plot of N-MgO@Fe₃O₄ nanosheet (b), DRS analysis (c) and Tauc′s plots (d) of N-MgO@Fe₃O₄ nanocomposite, and EIS Nyquist plots of the as-made catalyst N-MgO@Fe₃O₄ under dark and light conditions (e and f).

For further compositional and chemical characterization of the as-prepared N-MgO@ Fe$_3$O$_4$ catalyst, XPS analysis was performed before and after the photodegradation of IMD molecules. As can be seen, from the survey spectrum results in Fig. 2a-f, the presence of Mg 2p, O 1 s, N 1 s, and Fe 2p was confirmed in the catalyst structure. In the case of Mg 2 s (Fig. 2a) before reaction, two peaks located at 47.9 and 48.35 eV can be introduced as MgCO$_3$ and MgO components [46,47]. As shown in Fig. 2c, the O 1 s spectrum of the as-prepared N-MgO@Fe$_3$O$_4$ catalyst is composed of two peaks, at 530.3 and 531 eV, which are assigned to Fe-O bonding and lattice oxygen of MgO, respectively [48,49]. Based on Fig. 2e, the deconvolution of the Fe 2p spectrum in the fresh catalyst indicated peaks of Fe 2p$_{3/2}$ at 713 eV and Fe 2p$_{1/2}$ at 723 and 729 eV which were dedicated to Fe^{3+}, Fe^{2+} and Fe^{3+}, respectively [50,51]. As can be seen in Fig. 2g, the N 1 s spectrum of fresh catalyst was decomposed into three peaks at 397.8, 399.8, and 402.3 eV which were assigned to replacement of oxygen atom by N (Mg-N), amines group (N-H bonds) and adsorption of N atoms on MgO surface (N-O), respectively [52].

Porosimetry and specific area estimation of the as-prepared nanocomposite were measured by the BET technique. Based on Fig. 3a, the surface area, total pore volume (p/p$_0$ =0.99), and mean pore diameter of N-MgO@Fe$_3$O$_4$ nanosheets were determined to be 66 m^2/g, 0.39 cm^3/g, and 23 nm, respectively. Based on the curve results (BJH plot) and IUPAC classification, the isotherm of the as-prepared N-MgO@Fe$_3$O$_4$ was type IV, which indicates a mesoporous structure. In addition, this scale of material molecules can be beneficial for oxygen transfer and enhanced photocatalytic reactions [53]. As shown in Fig. 3b, the magnetization property of as-synthesized nano-catalyst was characterized by the VSM method and found between − 10,000–10,000 Oe. The obtained results estimate the magnetic value of N-MgO@Fe$_3$O$_4$ at about 7.1 emu/g. According to the literature, the magnetization of pure MgO is 1.03 emu/g [54], a significantly lower magnetization effect than the as-made catalyst in this work, which confirms the magnetite anchoring on the oxide. The presence of Fe$_3$O$_4$ in the structure of N-MgO@Fe$_3$O$_4$ (8 wt%) enhanced the magnetic property of the catalyst and effectuated easy separation of the catalyst from the reaction solution under a regular magnetic field (see the photo in inset Fig. 3b).

Furthermore, Fig. (3c-d) depicts the DRS results of N-MgO applied for determining the bandgap energy (E$_g$) of the as-made samples using Eqs. (2 and 3).

$$Eg = 1240/\lambda \quad (2)$$

$$(A h \upsilon) = \alpha \, (h\upsilon - Eg)n/_2 \quad (3)$$

where λ is the wavelength (nm) adsorption edge of samples, and A, h, υ, and α are constant values; the Plank's constant, light frequency, and absorption coefficient, respectively [11]. The values of Eg were calculated from the slope of $(\alpha h \upsilon)^2$ vs. $h\upsilon$ (eV) plot to be 2.7 eV for N-MgO (Fig. 3d). Considering the wide bandgap of MgO [21], it is shown that doping nitrogen atoms into the lattice structure of MgO considerably narrowed its bandgap, resulting in shifting the light absorption towards the visible region and thus improving the visible light photo-activity of MgO in the composite.

Fig. (3e-f) compares the EIS spectra of the as-synthesized MgO, N-MgO, and N-MgO@Fe$_3$O$_4$ catalysts. The catalysts had a smaller arc radius under light irradiation than in dark conditions. In addition, N-MgO either as a single catalyst or in the composite with Fe$_3$O$_4$ transferred a higher current and had a smaller arc radius than plain MgO. This can be attributed to the reduction of bandgap after N doping and the favorable crystalline structure of the catalyst [55]. It also means that in the N-MgO-containing catalysts, the production of carrier agent pairs including holes and electrons was accelerated under light, and doping MgO with N atoms could inhibit the electron-hole recombination and enhance electron transfer. In addition, it should be noted that the presence of Fe$_3$O$_4$ (containing both Fe^{2+} and Fe^{3+} ions) in N-MgO,

corresponded to a lower recombination rate of photoinduced agents (h^+, e_-)) [55].

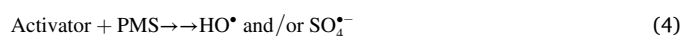## 3.2. Catalytic activity of N-MgO@Fe$_3$O$_4$: process parametrization

3.2.1. Effect of solution pH on the photocatalytic degradation of IMD

The effect of solution pH on IMD removal in the N-MgO@Fe$_3$O$_4$/PMS/light process is shown in Fig. 4a. The IMD degradation yield was 69%, 76%, 51%, and 45% for pH of 4, 5.6, 7, and 9, respectively, after 30 min. Based on the results, increasing pH towards alkaline conditions decreases IMD degradation efficacy. Thus, we report that pH= 5.6 was ideal for this system. This value is derived from the following facts:

i) The pH$_{pzc}$ of N-MgO@Fe$_3$O$_4$ was calculated at about 8.5, which revealed the catalyst surface was positively charged below that.

ii) IMD pKa1 = 1.6 and pKa2 = 11.1, meaning that it is in non-ionized form in the solution with the selected pHs.

iii) In addition, the pKa of PMS is 9.4, which means that it is negatively charged at a pH lower than 9.4, and the main species of HSO$_5^-$ will be formed in the solution [56]. In this condition, the interaction of catalyst surface with PMS species can be simplified the activation process toward increasing removal efficiency at acidic pH. As can be seen in Fig. 4a, the final pH for 7 reached 9.2, which could be attributed as an important reason for decreasing efficiency at this pH.

iv) In an alkaline solution the presence of OH$^-$ leads to a reaction with SO$_4^{\bullet-}$ which eventually generates HO$^\bullet$ radicals [56]. It should be noted that HO$^\bullet$ is non-selective with a short lifetime compared to SO$_4^{\bullet-}$ resulting in low degradation yield at pH= 9 [57].

v) Therefore, given that the $k_{SO_4^{\bullet}}^{IMD} = 3 \pm 1 \times 10^8$ M^{-1}s^{-1} at pH 6.02–8.64 [58] and $k_{HO^{\bullet}}^{IMD} = [2.7$–$3.8] \times 10^9$ M^{-1} s^{-1} at pH 6.02–7.92 [59,60], the last point (i.e., point iv) is not a drawback, but rather explains the higher "acidic" efficacy, compared to the alkaline conditions.

3.2.2. Effect of PMS presence/absence on IMD degradation in the N-MgO@Fe$_3$O$_4$/Visible light process: photocatalytic IMD degradation vs. PMS activation

The effect of adding different amounts of PMS to the N-MgO@Fe$_3$O$_4$/Visible light photocatalytic process in IMD degradation was investigated and the results are shown in Fig. 4b,c. IMD degradation efficiency (and its rate) in the photocatalytic process in the absence of PMS was 32% (0.007 min^{-1}) within 60 min, while it improved to 37% (0.009 min^{-1}) when 25 mg/L PMS was added to the reaction. Further increase in PMS concentration in the photocatalytic process to 50 and then 75 mg/L led to improvement of IMD degradation to 52.2% (0.013 min^{-1}) and 88.4% (0.037 min^{-1}), respectively, confirming the dominant role of PMS on IMD removal efficiency. The improvement of IMD degradation in the photocatalytic process in the presence of PMS can be related to the increased production of HO$^\bullet$ as well as to the formation of SO$_4^{\bullet-}$ from the PMS activation in the photocatalytic process by Eq. (4). SO$_4^{\bullet-}$ can also react with water molecules to form more HO$^\bullet$ through (Eq. 5) [61]. The greater amount of PMS concentration up to the optimum level, the higher the radical formation potential and thus the greater IMD degradation percentage.

$$\text{Activator} + \text{PMS} \rightarrow \rightarrow \text{HO}^\bullet \text{ and/or SO}_4^{\bullet-} \quad (4)$$

$$\text{SO}_4^{\bullet-} + \text{H}_2\text{O} \rightarrow \text{HO}^\bullet + \text{SO}_4^{2-} + \text{H}^+ \quad (5)$$

However, the IMD degradation decreased to 59.1% (0.016 min^{-1}) when the concentration of PMS was increased to 100 mg/L. Additional PMS beyond the optimum level could act as self- scavenging of main radicals that recombine to less oxidative species, forming weaker radical species like SO$_5^{\bullet-}$ (E^0 = 1.1 V) and HO$_2^\bullet$ (0.1 V) resulting in inhibiting the
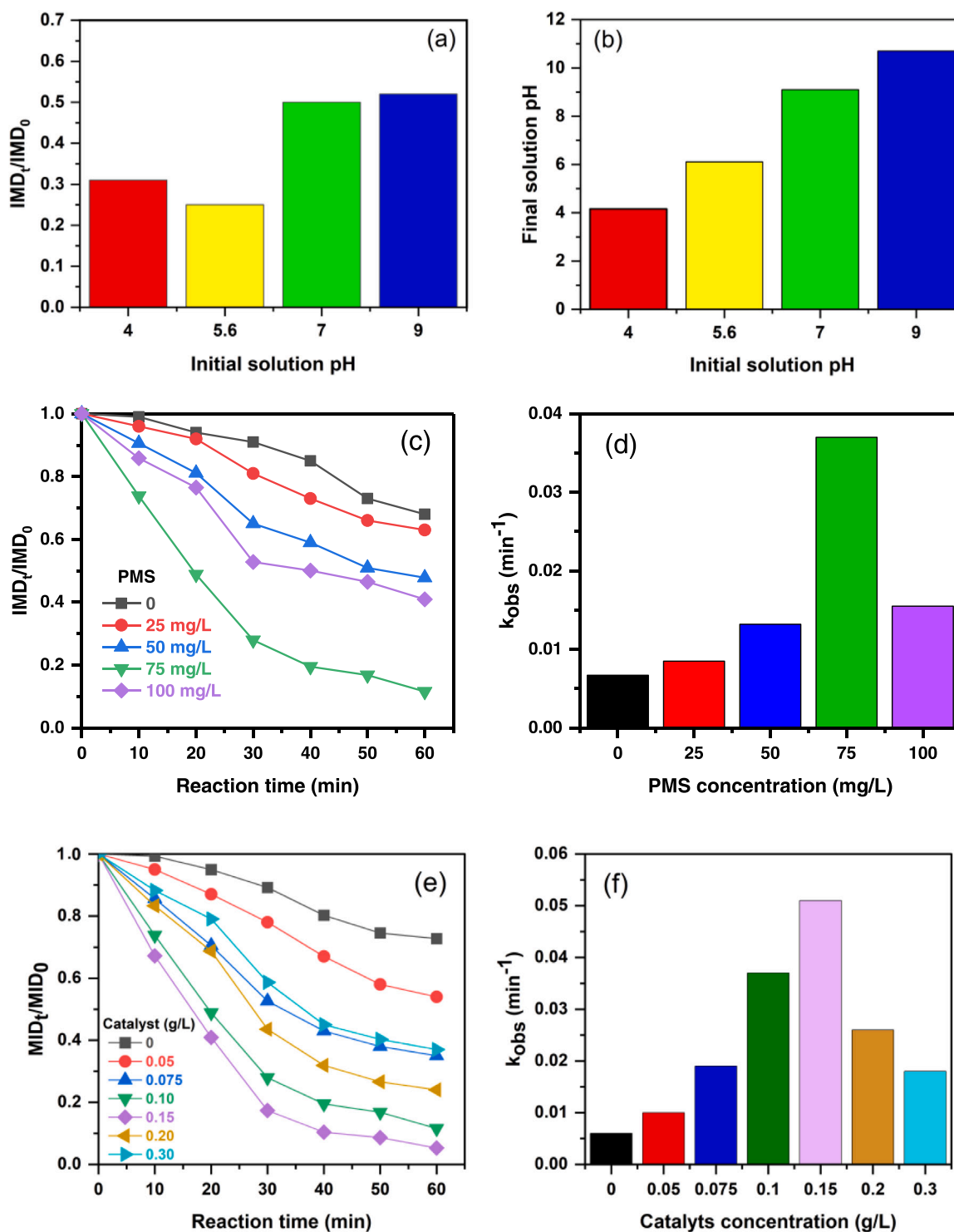
Fig. 4. Effect of solution pH on IMD degradation in the N-MgO@Fe$_3$O$_4$/PMS system (a) and pH changes during testing (b) (10 mg/L IMD, PMS concentration=75 mg/L, catalyst dosage=100 mg/L, reaction time=30 min). Effect of PMS concentration on IMD degradation efficiency (c) and rate (d) in the N-MgO@Fe$_3$O$_4$/VL process (IMD=10 mg/L, pH=5.6, catalyst=100 mg/L). Effect of N-MgO@Fe$_3$O$_4$ concentration on IMD removal percentage (e) and reaction rate constant (f) (IMD=10 mg/L, pH=5.6, PMS=75 mg/L).

degradation process, as proposed by Eqs. (6–10). Besides, overdosing on PMS can reduce the rate of reactions due to the saturation of catalyst active sites [34,62,63].

$$SO_4^{\bullet-} + SO_4^{\bullet-} \rightarrow S_2O_8^{2-} \tag{6}$$

$$HO^{\bullet} + HO^{\bullet} \rightarrow H_2O_2 \tag{7}$$

$$HO^{\bullet} + SO_4^{\bullet-} \rightarrow HSO_5^- \tag{8}$$

$$HSO_5^- + SO_4^{\bullet-} \rightarrow SO_4^{2-} + SO_5^{\bullet-} + H^+ \tag{9}$$

$$HO^{\bullet} + HSO_5^- \rightarrow SO_5^{\bullet-} + H_2O \tag{10}$$

3.2.3. Effect of N-MgO@Fe₃O₄ concentration on IMD degradation

The effect of N-MgO@Fe$_3$O$_4$ concentration between 0.05 and 0.3 g/L on catalytic degradation of 10 mg/L IMD in the VL/PMS-assisted process was investigated at a PMS concentration of 75 mg/L, solution pH of 5.6, and the results are shown in Fig. 4d-e. As can be observed in Fig. 4d, only 27.3% of IMD could be degraded with k_{obs} value of 0.006 min^{-1} within 60 min reaction time in the non-catalytic VL/PMS process. The relatively low IMD removal in the VL/PMS process can be related to the inefficacy of low-energy visible light photons used in the present study to activate PMS and thus to the less reactive species generated in the process [11]. Adding N-MgO@Fe$_3$O$_4$ at concentrations up to 150 mg/L to the VL/PMS process accelerated the IMD degradation up to 94.7% within 60 min (0.052 min^{-1}). This effect can be ascribed to the increased abundance of active reaction sites on the catalyst's surface resulting in the acceleration of photochemical reactions and thereby reactive species formation based on Eqs. 11 and 12. On the other hand, the synergistic effect between the N-MgO@Fe$_3$O$_4$ and PMS (Eq. 13) can photo-catalytically activate PMS and produce further SO$_4^{\bullet-}$ during the reaction [64]. The oxidation of PMS to generate SO$_5^{\bullet-}$ is also thermodynamically possible but given that the concentration of water is orders of magnitude higher than the PMS, it is not expected to affect considerably the process.

$$N-MgO@Fe_3O_4 \xrightarrow{h\upsilon} e^- + h^+ \tag{11}$$

$$h^+ + OH^- \rightarrow HO^\bullet \tag{12}$$

$$HSO_5^- + e^- \rightarrow HO^- + SO_4^{\bullet-} \quad \textbf{or} \quad HSO_5^- + h^+ \rightarrow SO_5^{\bullet-} + H^+ \tag{13}$$

When the concentration of the catalyst was further increased to 200 and then 300 mg/L, the degradation of IMD decreased to 76% (0.026 min^{-1}) and 63% (0.018 min^{-1}) under similar conditions (Fig. 4d). The decrease in the performance of the process at increased catalyst concentration can be attributed to the accumulation of nanoparticles in the suspension that led to the increase in the turbidity of the reaction medium and prevented the penetration of photons. This can limit the photocatalytic interactions and thus the formation of reactive radicals resulted in decreasing the IMD degradation percentages [11].

It should be noted that with increasing the concentration of catalyst, the amount of active surface sites increases and as a result, the presence of ROS species will be higher, so self-quenching of these species might be occurred based on Eqs. (6) and (7). The agglomeration of catalyst particles might cause this effect [34,65]. Based on the findings shown in Fig. 4d.e, the optimum experimental concentration of N-MgO@Fe$_3$O$_4$ in

the N-MgO@Fe$_3$O$_4$/VL/PMS process was 150 mg/L.

The visible-light activity of N-MgO@Fe$_3$O$_4$ material made in the present study to degrade IMD was compared with previously reported catalysts in the literature (Table 1). The catalytic potential of the as-made N-MgO@Fe$_3$O$_4$ material was compared with the relevant heterogeneous results reported, based on the pseudo-first-order reaction constant (k_{obs}) and rate (r_{obs}) calculated from Eqs. (14) and (15), respectively, as a normalization measure.

$$\ln\left(\frac{C_0}{C_t}\right) = k_{obs}.t \tag{14}$$

$$r_{obs} = k_{obs}.C_0 \tag{15}$$

C_o and C_t in the Eqs. (14) and (15) represent the IMD or TOC concentrations at the beginning and time t of the reaction.

Considering the values of r_{obs} for the degradation of IMD given in Table 1 for different catalysts, we confirm that the N-MgO@Fe$_3$O$_4$ had a superior performance among most of the other reported catalysts for IMD degradation, considering the operation conditions (in terms of catalyst concertation, type of light source, and light intensity). We note, however, that the higher values of r_{obs} reported in some of the studies summarized in Table 1 are those obtained employing higher amount of catalyst, higher light intensity, and/or mercury UV lamps, with potential severe secondary environmental pollution. In the other words, we observed a considerable photocatalytic r_{obs} value for the N-MgO@Fe$_3$O$_4$ irradiated with visible light under relatively mild conditions.

3.2.4. Elucidating the catalytic activity of the prepared materials and synergies among the constituents of the N-MgO@Fe₃O₄/PMS/VL process

The photocatalytic activity of the prepared materials (Fe$_3$O$_4$, MgO, N-MgO, MgO@Fe$_3$O$_4$, and N-MgO@Fe$_3$O$_4$) under visible light, and the efficacy in activating PMS, and catalyzing the VL/PMS process were investigated with IMD removal activity index, and the results are depicted in Fig. 5. As shown in Fig. 5, all the as-synthesized materials presented low IMD adsorption; the adsorption efficiency of IMD onto Fe$_3$O$_4$, MgO, N-MgO, MgO@Fe$_3$O$_4$, and N-MgO@Fe$_3$O$_4$ materials was 13.1, 19.1, 21.0, 22.3, 24.1%, respectively, at the contact time of 60 min under the selected conditions. It is observed that compositing Fe$_3$O$_4$ with MgO or N-MgO did not considerably affect its adsorption properties (Fig. S3). The visible-light photocatalytic activity of the as-synthesized materials was also investigated and the IMD removal was found to be 18.1, 25.0, 48.1, 23.2, and 57.8% in the photocatalytic process with Fe$_3$O$_4$, MgO, N-MgO, MgO@Fe$_3$O$_4$, and N-MgO@Fe$_3$O$_4$, respectively. It

Table 1
Comparison of the photoactivity of N-MgO@Fe₃O₄ in comparison with other catalysts used for IMD degradation.

| Catalyst	Experimental conditions					Degradation		Mineralization		Ref.
Type	Conc. (g/L)	Light/W	IMD (mg/L)	pH	Time (min)	Percentage (%)	Rate (mg/L. min)	Percentage (%)	Rate (mg/L. min)	
g-C$_3$N$_4$	0.05	VL/300 W	20	7	300	90	0.13	–	–	[3]
Z- WO$_3$/polyimide	1	VL/225 W	20	7	180	73.2	0.07	–	–	[6]
OCN-10/PMS	0.5	Xe/500 W	3	4.2	120	94.5	0.075	41.6	–	[7]
TiO$_2$	1	UVA/15 W	25	9	20	100	–	30	–	[60]
TiO$_2$	0.24	UVA/120 W	100	7	120	98.8	3.50	19.1	–	[66]
TiO$_2$/H-ZSM-5	1	Xe/100 W	10	7	40	96.4	0.69	–	–	[67]
TiO$_2$	1.5	UVA/15 W	10	6.5	240	83.6	0.07	–	–	[68]
H$_3$PW$_{12}$O$_{40}$/ TiO$_2$–n$_2$O$_3$	3.6	VL/225 W	8	7	318	83	0.04	–	–	[69]
H$_3$PW$_{12}$O$_{40}$/La-TiO$_2$	0.6	Xe/300 W	10	5	60	98.2	0.74	–	–	[70]
Ferrioxalate reagent	0.24	UVA /9 W	20	3.2	120	90	–	85	–	[71]
GO/CuFe$_2$O$_4$-CdS	10	tungsten/ 300 W	10	8	100	100	0.62	–	–	[72]
Au–SnO2–CdS	0.003	LED/30 W	1	4	180	95	0.02	–	–	[73]
N-MgO@Fe$_3$O$_4$	0.15	VL/24 W	10	5.6	60	57.8	–	–	–	This study
N-MgO@Fe$_3$O$_4$/PMS	0.15	VL/24 W	10	5.6	60	94.7	0.52	63.8	0.25	This study
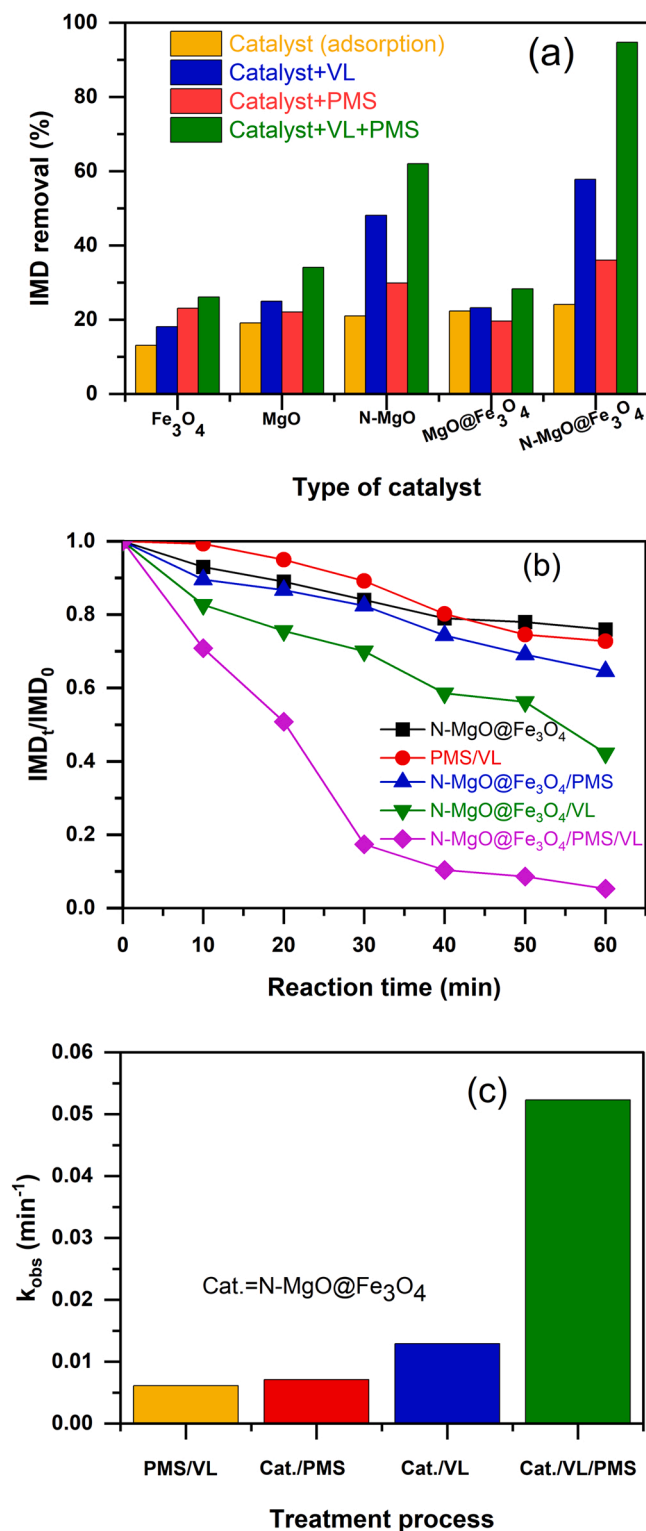
Fig. 5. The catalytic activity of as-made catalysts at the reaction time of 60 min (a), and kinetics (b,c) of the best-performed processes in removing IMD (IMD=10 mg/L, pH = 5.6, catalyst=0.15 g/L, PMS =75 mg/L]; (The IMD removal using single VL and PMS was around 1% and 6%, respectively).

is observed in Fig. 5a that the photocatalytic activity of N-MgO was around x2 times higher than that of MgO under similar experimental conditions, confirming that doping MgO with nitrogen considerably increased its activity under visible light. The improved photocatalytic activity of N-MgO can be attributed to its lower bandgap, utilized under

visible light. Indeed, MgO has a wide bandgap and when it was doped with N (making N-MgO) the new bandgap above the valence band obtained about 2.7 eV (Fig. 3c-d), which in turn could improve its light-harvesting capacity and accelerate its photo-activity [54]. This phenomenon can be related to the species of N such as N_0^0 and N_0^- according to (Eqs. 16 and 17) [74]. Furthermore, considering the XPS results, the N dopant replaced oxygen atoms in the MgO lattice to form oxygen defects and increased the separation yield of electron-hole pairs on the MgO surface, so it possibly prevents the recombination of photogenerated agents and thus enhances the photocatalytic activity [28,74].

$$N_0^- + e^- \rightarrow N_0^0 \tag{16}$$

$$N_0^0 + e^- \rightarrow N_0^- \tag{17}$$

In addition, comparing the photocatalytic activity of MgO and N-MgO materials with those of their composited form with Fe_3O_4 shown in Fig. 5a, depicts that Fe_3O_4 slightly decreased the visible light photocatalytic activity of MgO catalyst. It can be related to low optical behavior and thus the low photocatalytic activity of Fe_3O_4 under the selected condition (Fig. 5a), as well as to the long bandgap of the MgO. In contrast, compositing Fe_3O_4 with N-MgO considerably improved its photocatalytic activity by 20% (57.8% in the N-MgO@Fe_3O_4/VL to 48.1% in the N-MgO/VL processes). This improvement is shown because N-MgO has a low bandgap thus the transfer of charge carriers between N-MgO and Fe_3O_4 can affect the photocatalytic behavior of the N-MgO@Fe_3O_4 catalyst (see below, Fig. 6). Indeed, due to the difference between energy gaps, a part of the h^+ formed in the VB of N-MgO could transfer to the VB of Fe_3O_4 and the e^- in CB of Fe_3O_4 migrated to the CB of N-MgO [32,49]. It resulted in improving the separation of the electron-hole pairs generated in N-MgO and Fe_3O_4 materials present in the composite, thus forming more reactive species including $HO^\bullet$ (Eqs. 13 and 14), led to an increase in IMD removal.

Therefore, considering the negligible IMD removal using direct photooxidation by visible-light photons and only 20.8% adsorption of IMD onto N-MgO@Fe_3O_4 (Fig. 5a), achieving 57.8% of IMD removal in the visible-light photocatalytic process with N-MgO@Fe_3O_4 confirms the high activity of the as-made catalysts with a noticeable synergy between visible-light and N-MgO@Fe_3O_4. In parallel, synergy was not observed between the visible light and the MgO@Fe_3O_4, reconfirming the role of doping MgO with N in considerably improving its catalytic activity under visible light irradiation.

Furthermore, the potential of the prepared materials for activation of PMS was also evaluated and the results are included in Fig. 5a. It is observed in Fig. 5a that the N-MgO@Fe_3O_4 had the highest potential for activation of PMS among the tested materials; 35.4% of IMD was removed in the N-MgO@Fe_3O_4/PMS process, whereas it was 22.1% in the MgO/PMS, 29.9% in the MgO@PMS, and MgO@Fe_3O_4/PMS processes under the same selected conditions. In comparison, the performance of the MgO@Fe_3O_4/PMS process in removing IMD was 19.6% under the same experimental conditions. Therefore, the behavior of the prepared materials in catalyzing PMS was similar to that of their photocatalytic activity, i.e., the N-MgO had higher potential than the MgO in catalyzing PMS, and N-MgO@Fe_3O_4 had higher potential than the N-MgO in catalyzing PMS. It is seen in Fig. 5a that doping MgO with N, in addition to improving the photocatalytic activity, could also increase its catalytic potential in the activation of PMS, since IMD removal in the N-MgO/PMS process was 1.4 times that in the MgO/PMS one.

Also, the as-made catalyst easily adsorbed the negative form of PMS, resulting in high photogenerated electron transfer from the catalyst surface to oxidant and its effective activation to form reactive radical species [75]. In addition, the presence of N in the catalyst might promote the activation of PMS through a non-radical mechanism by producing $^1O_2$ [37], as shown in Eq. (18).

$$2SO_5^{\bullet-} + H_2O \rightarrow 2HSO_5^- + {}^1O_2 \tag{18}$$
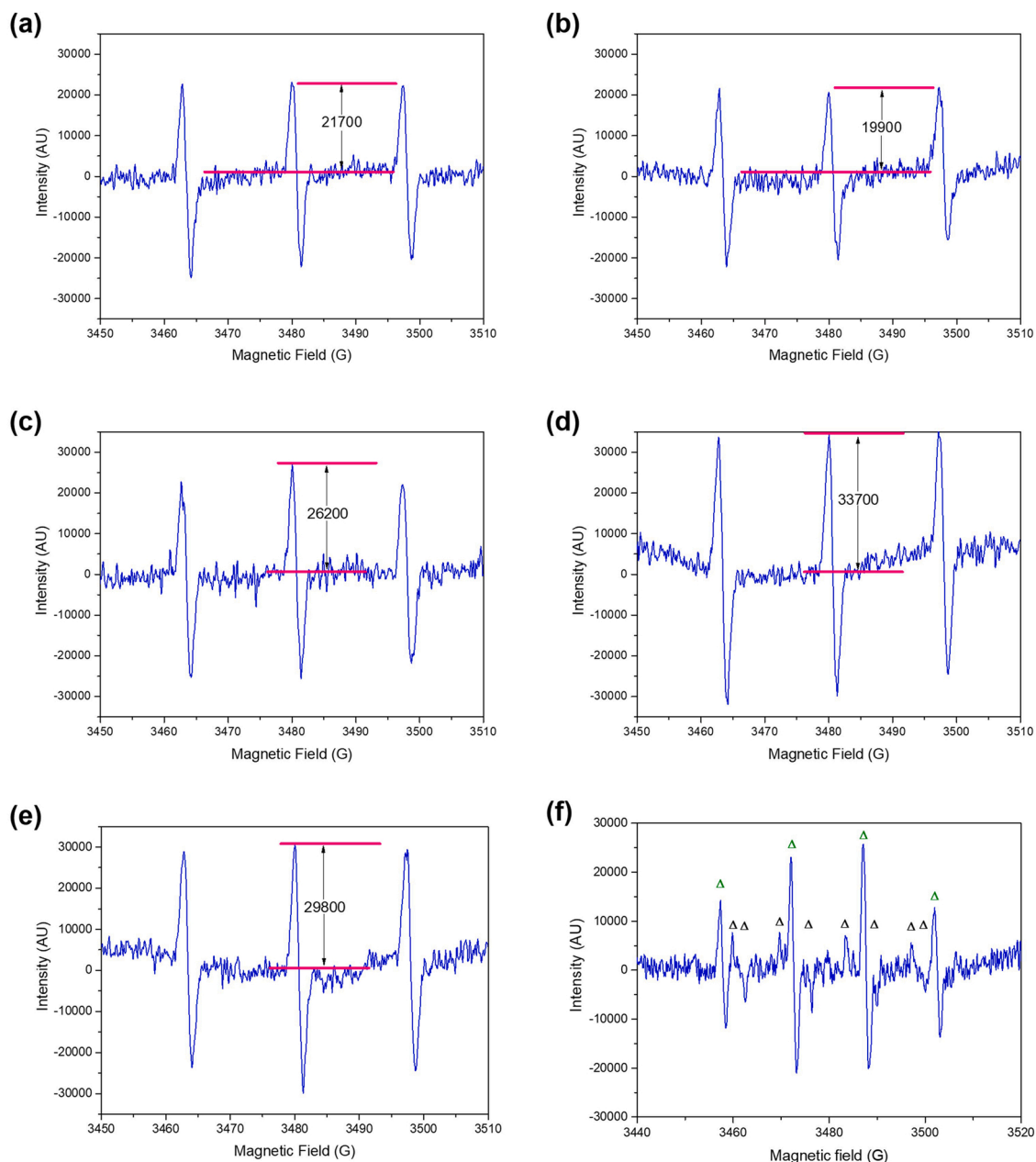
Fig. 6. EPR spectra recorded in aerated D_2O upon irradiation (Xe lamp with a 380 nm cut-off filter) of: a) no photocatalyst or oxidant; b) N-MgO@Fe$_3$O$_4$ (150 mg/L); c) PMS (75 mg/L); d) N-MgO@Fe$_3$O$_4$ (150 mg/L) and PMS (75 mg/L); e) N-MgO@Fe$_3$O$_4$ (150 mg/L) and PMS (75 mg/L) in dark. TEMP (1.2 mM) was used in (a-e) as a spin trap. (f) EPR experiment of an aqueous deaerated mixture of DMPO (10 mM), N-MgO@Fe$_3$O$_4$ (150 mg/L), and PMS (75 mg/L) at pH ca. 6 under Xe lamp irradiation (a 435 nm cut-off filter was employed). Black symbols correspond to the DMPO-SO$_4$ signal and green symbols correspond to the DMPO-OH signal.

Moreover, although Fe$_3$O$_4$ showed low optical behavior, its anchoring on N-MgO had some synergistic effect on PMS activation. As per Fig. 5a, the N-MgO@Fe$_3$O$_4$ material had the highest visible-light photocatalytic property as well as the highest potential for activating PMS, among the as-prepared materials. Therefore, the mutual catalyti-cally benefit of the N-MgO@Fe$_3$O$_4$ as a visible-light photocatalyst and as a PMS activator was investigated. Another interesting point found in Fig. 5a is that adding PMS to the VL/N-MgO@Fe$_3$O$_4$ photocatalytic process resulted in further improvement of the IMD removal from 57.8% to 94.7%, under the selected conditions. Considering the point that IMD removal in the VL/PMS process was around 27.3%, and the results given in Fig. 5a, considerable synergy in IMD removal was achieved when N-MgO@Fe$_3$O$_4$ was added to the VL/PMS process. To understand the visible-light catalytic activity of N-MgO@Fe$_3$O$_4$ and the effect of PMS on boosting the performance of the N-MgO@Fe$_3$O$_4$/VL photocatalytic

process in the degradation of IMD, the kinetics of these processes were evaluated (Fig. 5b) and compared in terms of the value of k$_{obs}$ (Fig. 5c). It was found that the VL/PMS, N-MgO@Fe$_3$O$_4$/PMS, N-MgO@Fe$_3$O$_4$/VL, and N-MgO@Fe$_3$O$_4$/VL/PMS processes removed IMD at the PFO rate constants of 0.006, 0.007, 0.013, and 0.052 min^{-1}, respectively, under the selected conditions. Accordingly, a synergy factor of 2 was calculated from Eq. (19) for the process developed from coupling the N-MgO@Fe$_3$O$_4$, PMS activation, and visible light irradiation in removing IMD.

$$\text{Synergy } factor = \frac{k_{obs}[\text{catalyst/VL/PMS}]}{k_{obs}[\text{catalyst/VL}) + k_{obs}[\text{catalyst/PMS}] + k_{obs}[\text{VL/PMS}]}$$
(19)

Furthermore, the N-MgO@Fe$_3$O$_4$ with a high optical property could be excited under visible light, resulting in the photogeneration of e$^-$ and

h^+ according to Eq. (11); these photogenerated species could then counterpart in activating PMS with the subsequent formation of $SO_4^{•-}$ and $HO^•$ (Eqs. 12 and 13). Specifically, the activation of PMS could be accelerated by contributing conduction electrons based on Eq. (13). PMS acted as an electron acceptor reducing the recombination rate of photoinduced agents and giving rise to $SO_4^{•-}$, a reactive species that could enhance IMD removal efficiency. Moreover, conduction electrons could also reduce O_2 to $O_2^{•-}$ (Eq. 22), that eventually could either participate in the degradation of IMP or result into $^1O_2$, an additional reactive species. In addition, even without visible light irradiation, Fe^{3+} could react with PMS for the formation of Fe^{2+} producing $SO_5^{•-}$ and then active sites of Fe^{2+} can activate PMS to produce more $SO_4^{•-}$ [34,63].

$$Fe^{3+} + HSO_5^- \rightarrow Fe^{2+} + H^+ + SO_5^{•-} \quad (20)$$

$$Fe^{2+} + HSO_5^- \rightarrow Fe^{3+} + HO^- + SO_4^{•-} \quad (21)$$

$$e^- + O_2 \rightarrow O_2^{•-} \quad (22)$$

MgO as a non-redox active oxide might change the coordination environment of Fe, thus changing the direction of the transfer of a photogenerated electron between PMS and transition metal, and thus inducing $^1O_2$ generation. Finally, molecular IMD could be degraded in the N-MgO@Fe$_3$O$_4$/VL/PMS process by reactive species formed through a chain of reactions, simplified in Eq. (23), to simple intermediates [49].

$$IMD + \left[SO_4^{•-} + HO^• + O_2^1 + h^+ + O_2^{•-} \right] \rightarrow product \quad (23)$$
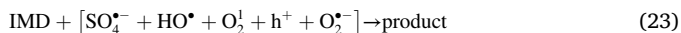
3.2.5. Evidence on the formation of reactive species: EPR study

EPR experiments were carried out to shed light into the photogeneration of the potential reactive species ($HO^•$, $SO_4^{•-}$, $^1O_2$ and $O_2^{•-}$) upon irradiation of the complex system formed by N-MgO@Fe$_3$O$_4$ and PMS, which eventually could participate in the degradation of IMD. First, EPR experiments were conducted in the presence of a radical spin trap of $^1O_2$ (TEMP, 1.2 mM), which results in the formation of a stable TEMPO radical with a well-known pattern signal [42]. The formation of $^1O_2$ was explored in the presence of N-MgO@Fe$_3$O$_4$ (150 mg/L) and PMS (75 mg/L) in aerated D$_2$O at pH ca. 6 under Xe lamp irradiation (a 380 nm cut-off filter was employed). Control experiments in which only TEMP was employed and in the presence of only N-MgO@Fe$_3$O$_4$ (150 mg/L) or PMS (75 mg/L), all in aerated D$_2$O were performed in parallel (Fig. 6a-c). Results showed the formation of the typical TEMPO signal in all cases, although the highest intensity of TEMPO was found when N-MgO@Fe$_3$O$_4$ and PMS were irradiated together (Fig. 6. d). The formation of TEMPO in the presence of only N-MgO@Fe$_3$O$_4$ or PMS is attributed to the initial TEMP oxidation (TEMP$^{•+}$), followed by subsequent deprotonation and reaction with O$_2$. This process has been described for aerated TEMP mixtures in the presence of other oxidants [76]. Nevertheless, from the comparison of the intensity of the TEMPO signal formed within the control mixtures and in the presence of N-MgO@Fe$_3$O$_4$ and PMS, ca. 10% of the signal intensity can be safely attributed to the formation of $^1O_2$. To further confirm the formation of $^1O_2$ an additional experiment was carried out in which the decrease in the absorbance of the probe anthracene 9,10-dicarboxylic acid was attributed to the initial formation of an oxetane [77], according to the Fig. S4. Thus, a mixture of anthracene 9,10-dicarboxylic acid (23 μM), N-MgO-Fe$_3$O$_4$ (150 mg/L), and PMS (75 mg/L) was irradiated (Xe lamp coupled with a 380 nm cut-off filter) in parallel in H$_2$O and D$_2$O, see Fig. S5 left and right, respectively. The higher decrease in the absorbance of anthracene 9,10-dicarboxylic acid when the experiment was carried out in D$_2$O vs H$_2$O was in agreement with the formation of $^1O_2$ with a lifetime one order of magnitude longer than in H$_2$O [42].

Furthermore, EPR experiments in the presence of DMPO (10 mM) were performed to provide evidence of the photogeneration of intermediates of radical nature such as $HO^•/SO_4^{•-}$ upon irradiation of deaerated aqueous mixtures of N-MgO@Fe$_3$O$_4$ (150 mg/L) and PMS

(75 mg/L) at pH ca. 6 (a 435 nm cut-off filter was employed). It is reported that both intermediates react efficiently with DMPO giving rise to DMPO-SO$_4$ and DMPO-OH, respectively. Results showed the typical signal patterns corresponding to DMPO-SO$_4$ and DMPO-OH (Fig. 6f), while no signals were obtained in the absence of irradiation (data not shown). The DMPO-SO$_4$ signal could be safely attributed to the trap of $SO_4^{•-}$ generated from the reduction of PMS according to Eqs. (13) and (21). On the other hand, the DMPO-OH signal could have two different origins: irradiation of N-MgO@Fe$_3$O$_4$ gives rise to the generation of vacancies in the valence band that can generate $HO^•$, according to Eq. (12); however, it is also known that the lifetime of the DMPO-SO$_4$ adduct in H$_2$O is very short, and quickly evolves to DMPO-OH [78]. Thus, the appearance of DMPO-OH does not represent unambiguous evidence for the direct formation of $HO^•$ in the photogenerated vacancies of the VB, or because of the ferric photo-reduction.

To provide further evidence on the photogeneration of $HO^•$, an additional experiment was carried out in which the non-emissive terephthalic acid gave rise to the emissive hydroxyterphthalate derivative [79], shown in Fig. S6. Thus, an aqueous mixture of terephthalic acid (50 mM), NaOH (2 mM), N-MgO-Fe$_3$O$_4$ (150 mg/L), and PMS (75 mg/L) was irradiated (Xe lamp coupled with a 380 nm cut-off filter) for up to 120 min ($\lambda_{exc} = 315$ nm, see Fig. S7). The results demonstrating the formation of the fluorescent derivative prove the previous suggestions for the formation of $HO^•$ in the process.

Furthermore, the excitation of electrons to the conduction band of the photocatalyst and the role of oxygen as electron acceptor may lead to the generation of superoxide radical anion ($O_2^{•-}$), according to Eq. 22. Attempts were made to trap the potentially formed $O_2^{•-}$ as DMPO-OOH. For this purpose, aerated aqueous mixtures of N-MgO@Fe$_3$O$_4$ (150 mg/L) and DMPO (10 mM) at pH ca. 6 were irradiated in the absence of PMS (a 320 nm cut-off filter was employed). However, no signals that could be attributed to the formation of DMPO-OOH were observed. Even more, the experiment was repeated in an ethanolic-aqueous mixture to quench the hydroxyl radical and enhance the prospects to detect DMPO-OOH. However, we did not observe any signal that could provide positive evidence on the formation of $O_2^{•-}$. This means that $O_2^{•-}$ is either not formed, or gets quickly transformed to other species, e.g., singlet oxygen (Eq. 24):

$$h^+ + O_2^{•-} \rightarrow O_2^1 \quad \text{or} \quad 2H^+ + 2O_2^{•-} \rightarrow O_2^1 + H_2O_2 \quad (24)$$
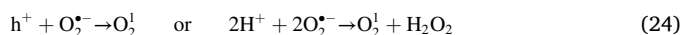
Hence, from the EPR experiments, we can provisionally conclude that the irradiation of mixtures of N-MgO@Fe$_3$O$_4$ and PMS in aerated aqueous media gives rise to the formation of $^1O_2$ (as was demonstrated when TEMP was used as a spin-trap), and to the formation of $SO_4^{•-}$ (as proven from the formation of DMPO-SO$_4$). The direct formation of $HO^•$ was proven from the formation of the fluorescent adduct of hydroxyterphthalate. Nevertheless, the results obtained did not allow quantification of the different species.

3.2.6. Mechanism of IMD degradation in the N-MgO@Fe$_3$O$_4$/VL/PMS process

To identify the type of species formed in the N-MgO@Fe$_3$O$_4$/VL/PMS process, IMD removal was compared in the absence and presence of several scavengers, such as p-benzoquinone (p-BQ), tert-butanol (TBA), ethanol (EtOH), sodium azide (SA) and oxalate (OX), as the scavengers of the photoproduced reactive intermediates formed and potentially IMD-degrading species (including $O_2^{•-}$, $HO^•$, $SO_4^{•-}$, $^1O_2$ and h^+). The results are shown in Fig. 7, demonstrating the inhibition of IMD removal percentage (Fig. 7a) and rate (Fig. 7b) in the presence of the selected scavengers. The percentage (rate) of IMD degradation in the N-MgO@-Fe$_3$O$_4$/VL/PMS process decreased from 94.7% (0.052 min^{-1}) under normal conditions, down to 77.6% (0.028 min^{-1}) in the presence of pBQ, or to 62.7% (0.018 min^{-1}) in the presence of OX, to 53.2% (0.012 min^{-1}) in the presence of TBA, to 35.9% (0.007 min^{-1}) in the presence of EtOH, and to 15.2% (0.003 min^{-1}) in the presence of SA
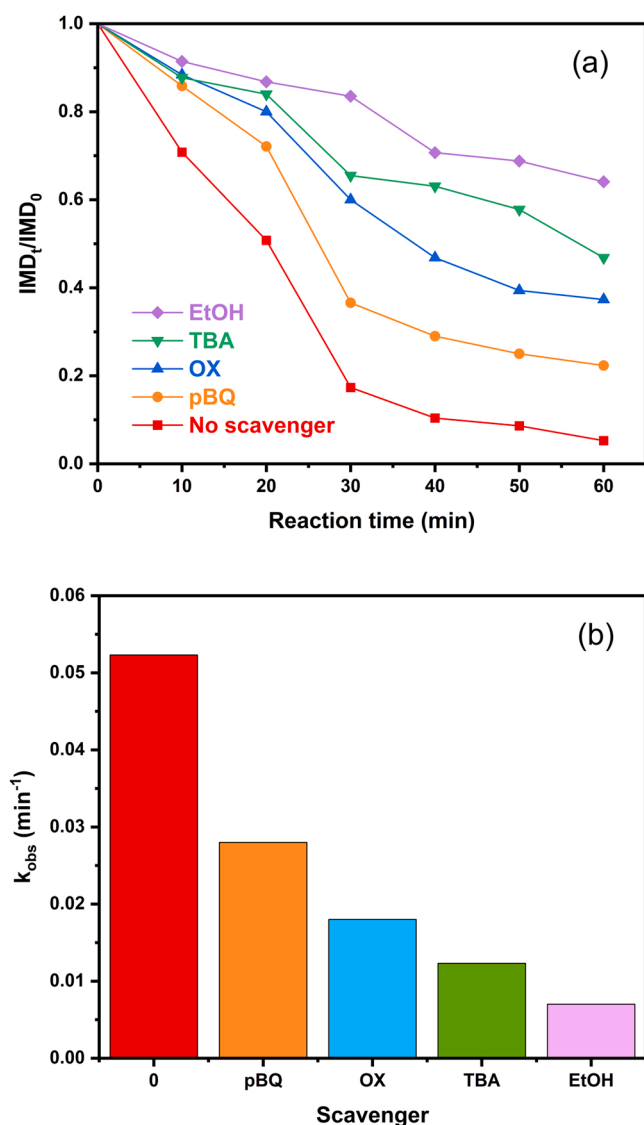
Fig. 7. Effect of different scavengers (a) and reaction rate constant (b) (IMD=10 mg/L, pH=5.6, PMS =75 mg/L, scavenger= 0.1 M, reaction time=0–60 min).

(Fig. 7a). Since the concentration of scavengers in the test was several orders of magnitude greater than that of IMD, it can be considered that all the reactions were run under saturated quenching conditions. Therefore, the inhibition order of scavengers on IMD degradation efficacy in the N-MgO@Fe$_3$O$_4$/VL/PMS process was as follows: SA>EtOH>TBA>OX>pBQ. It is found that TBA, EtOH, and SA had the highest inhibition effect on IMD degradation in the developed process. Thereby, by using OX in the IMD degradation can be observed that the photo-generated holes in the catalyst played a clear contribution in this process because OX would prevent the reaction between the holes and water molecules to generate HO$^\bullet$ [77]. The clear inhibition effect obtained in the degradation of IMD by the presence of EtOH and TBA as scavengers of HO$^\bullet$ and SO$_4^{\bullet-}$ suggests the participation of both radicals.

Moreover, IMD degradation results were deeply analyzed based on the bimolecular rate constants (k) of HO$^\bullet$ with EtOH, TBA, and IMD(k ca. 1.9×10^9, 6.0×10^8 and 2.7–3.8×10^9 M^{-1} s^{-1}, respectively), those described for SO$_4^{\bullet-}$ with EtOH, TBA, and IMD (k ca. 3.5×10^7, 4.0×10^5 M^{-1}s^{-1}, and $3 \pm 1 \times 10^8$ M^{-1}s^{-1}, respectively) [58,80], together with the typical reported values for the lifetime of SO$_4^{\bullet-}$ and HO$^\bullet$ (ca. 1 microsecond and 100 microseconds, respectively) [81,82]. Interestingly, if the main radical involved was HO$^\bullet$, the same decrease in

the degradation would have been observed in the presence of EtOH or TBA at concentrations as high as 0.1 M. Thus, the higher effect observed in the presence of TBA could be attributed to the participation of SO$_4^{\bullet-}$. However, the fact that the IMD degradation was not affected by increasing the quencher amounts of TBA and EtOH from 0.1 to 1 M (see Fig. S8), reveals the involvement of other reactive species in this process.

Based on the scavenging tests results, the IMD degradation resulted to be slightly lower by the presence of SA (Fig. S9) than that produced by the presence of EtOH (Fig. 7). This finding could be explained by the participation of a non-radical mechanism such as ^{1}O$_2$, which might have a role in IMD removal [49,81,82]. Thus, as SA reacts with HO$^\bullet$ and SO$_4^{\bullet-}$ with a rate constant of 1.2×10^{10}, 2.5×10^9 M^{-1}s^{-1}, respectively, but also with singlet oxygen (^{1}O$_2$) with a k ca. 2×10^9 M^{-1}s^{-1}, this last quenching reaction could explain the best inhibition produced by SA [83].

Nevertheless, since complete inhibition was not produced also using SA, it could indicate that O$_2^{\bullet-}$ might be participating in the IMD degradation. In this context, pBQ was used to prove this contribution but the results were not clear, because this quencher can not only scavenge superoxide anion at a rate of 1×10^9 M^{-1} s^{-1}, but also HO$^\bullet$ at a rate of 2.19×10^9 M^{-1} s^{-1} and SO$_4^{\bullet-}$ at 2.5×10^9 M^{-1} s^{-1}. However, the effects observed cannot be explained by considering only the concentration of pBQ used and its rate constants [84], and considering that we did not detect any EPR signal we suggest that its importance must not be critical. In overall, the mechanisms deduced to be involved in the degradation of IMD in the N-MgO@Fe$_3$O$_4$/VL/PMS process are presented in Fig. 8.

From the XPS analysis, the binding energy in the used catalyst (Fig. 2b) was centered at 50 eV, which can be related to the oxidation state of MgO, as Mg^{2+}. Also shifting the peak after reaction from 47.9 to 49.2 eV showed the formation of Mg(OH)$_2$ during the oxidation of surface carbonaceous materials [46,47]. After IMD degradation (Fig. 2d), a small change in the position of the peaks was observed for O 1 s at 531.3 and 532.2 eV, which can be assigned to the formation of Mg (OH)$_2$ and the adsorption of water molecules on the catalyst's surface, respectively [47–49]. In addition, a new peak at 710 eV observed in the catalyst after reaction (Fig. 2f) was assigned to Fe^{2+}, which demonstrated that Fe^{3+} has been partly reduced to Fe^{2+} [50,51]. It should be noted that the peaks at 397.8 eV vanished, and other peaks were shifted toward 399 and 407.2 eV in the catalyst after the reaction (Fig. 2h), which indicates the amine groups were decomposed during the photocatalytic process [52].

3.3. Assessing the N-MgO@Fe$_3$O$_4$ applicability: water matrix influence, stability & reusability, and IMD degradation pathways

3.3.1. Effect of competing anions presence on IMD photocatalytic degradation

The performance of common water anions, i.e., Cl$^-$, NO$_3^-$, HCO$_3^-$ and PO$_4^{3-}$ were evaluated on IMD degradation in the N-MgO@Fe$_3$O$_4$/ VL/PMS process. The experiment was also conducted for IMD removal in tap water as a matrix containing a mixture of these anions. As can be seen in Fig. 9a, Cl$^-$ and NO$_3^-$ did not considerably affect IMD degradation, indicating a slight quenching reaction with reactive species [58]. The small hindering effect of Cl$^-$ on the process can be related to the reaction between Cl$^-$and HSO$_5^-$ which transformed to HOCl and Cl$_2$ with lower redox potential than SO$_4^{\bullet-}$(Eqs. 25 and 26) [63], but possessing a small oxidative power that could still degrade/oxidize IMD.

$$HSO_5^- + Cl^- \rightarrow SO_4^{2-} + HOCl \tag{25}$$

$$HSO_5^- + 2Cl^- + H^+ \rightarrow SO_4^{2-} + Cl_2 + H_2O \tag{26}$$
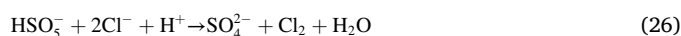
Similar to chloride, by adding NO$_3^-$ to the reaction medium, some species such as NO$_3^\bullet$ (2.3 eV) and NO$_2^\bullet$ (1.03 eV) can be formed with less oxidative potential compared to SO$_4^{\bullet-}$ and HO$^\bullet$ based on (Eqs. 27 and 28) that decreased IMD decomposition [63].
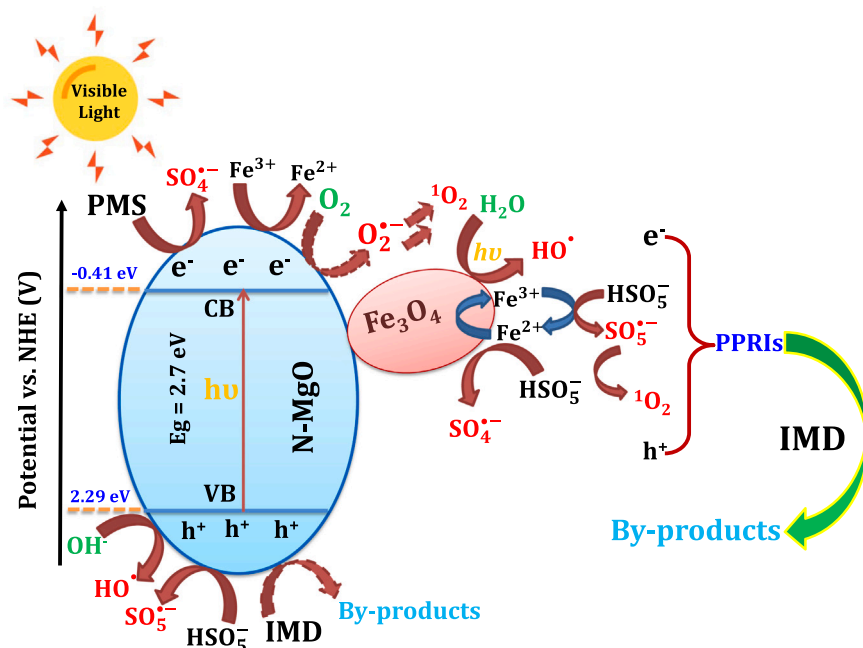
Fig. 8. Schematic diagram of IMD degradation by N-MgO@Fe$_3$O$_4$/VL/PMS process. PPRIs: photo-produced reactive intermediates. Arrows with dashed lines indicate probable but not detected/verified pathways.

$$NO_3^- + ROS \rightarrow NO_3^\bullet + OH^- / SO_4^{2-} \qquad (27)$$

$$NO_3^\bullet + H_2O + e^- \rightarrow NO_2^\bullet + 2OH^- \qquad (28)$$

However, the degradation of IMD was significantly inhibited by HCO_3^- and PO_4^{3-} so that it decreased from 94.7% in absence of anions to 44.5% and 56.2% in the presence of HCO_3^- and PO_4^{3-}, respectively, under the selected conditions. HCO_3^- reacts with $HO^\bullet$, $SO_4^{\bullet-}$ and h^+ resulting in the formation of $HCO_3^{\bullet-}$ and $CO_3^{\bullet-}$ species with lower redox potential (1.78 eV) through (Eqs. 29–31) [63,81,82].

$$HCO_3^- + HO^\bullet \rightarrow H_2O + CO_3^{\bullet-} \qquad (29)$$

$$HCO_3^- + SO_4^{\bullet-} \rightarrow SO_4^{2-} + HCO_3^{\bullet-} \qquad (30)$$

$$HCO_3^- + h^+ \rightarrow H_2O + CO_3^{\bullet-} \qquad (31)$$

Similarly, the addition of PO_4^{3-} exhibited a negative performance on the oxidation process by trapping radical agents (Eqs. 32 and 33). In addition, it could block the active sites on the catalyst surface and prevent to penetration of photons or the formation of a complex between PMS and N-MgO@Fe$_3$O$_4$ [85–87].

$$HPO_4^{2-} + HO^\bullet \rightarrow OH^- + H_2 + HPO_4^{\bullet-} \qquad (32)$$

$$HPO_4^{2-} + SO_4^{\bullet-} \rightarrow SO_4^{2-} + HPO_4^{\bullet-} \qquad (33)$$

Wang et al. [88] reported the same inhibition influence of anions for degradation of bisphenol A by the Ag-g-C$_3$N$_4$/PMS/visible light process. Another point observed in Fig. 9a is that the degradation of IMD in spiked tap water in the N-MgO@Fe$_3$O$_4$/VL/PMS process was 91.5%, deducing that the developed process was not highly influenced by the water matrix of natural water, thus it could perform well for treating mildly contaminated water sources. In addition, a slight reduction in IMD removal efficiency can be attributed to the high amount of TDS that can interfere with reactive species and trap them in the oxidation process, and the small reduction of water transmittance. Hence, the presence of anions in tap water in the standard range had no adverse effect on degradation reaction [63].
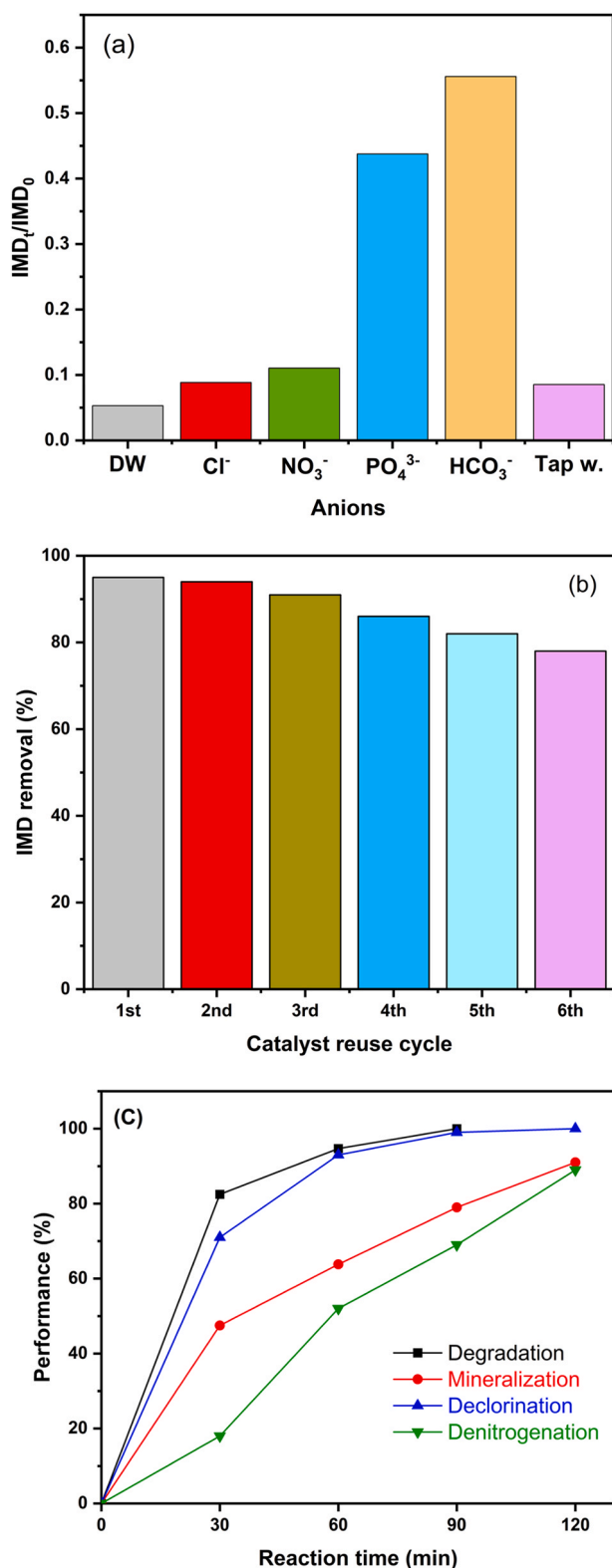
3.3.2. Recyclability and durability of N-MgO@Fe$_3$O$_4$ over repetitive cycles of IMD photocatalytic degradation

The recyclability of the prepared N-MgO@Fe$_3$O$_4$ material catalyzing the activation of visible light and PMS was examined for six consecutive runs and the results are shown in Fig. 9b. After six consecutive cycles of the catalyst reuse, an IMD removal of over 78% could still be achieved in the N-MgO@Fe$_3$O$_4$/VL/PMS process, indicating the slight reduction of degradation efficiency after the sixth reuse cycle and proving excellent recoverability of the catalyst. Within the first 5 cycles, the efficacy is within the margin of error, hence negligible differences are reported. From the 5th cycle and onwards, the relatively low deactivation of photocatalytic performance could be resulting from catalyst reduction during separation, loss of active catalyst surface sites by washing, and bond formation with by-products excluding penetrate light, PMS activation, and generation of ROS species [11,63]. From the point of economic view, the demonstrated efficient reusability is a critical property for its potential application.

For further confirmation, the sustainability of recovered N-MgO@-Fe$_3$O$_4$ was more evaluated by XRD, FTIR and TEM imaging and comparing the results before (Fig. 1) and after (Fig. S10). Fig. S10a depicts the XRD pattern of the reused N-MgO@Fe$_3$O$_4$ material, observing the main diffraction peaks of MgO and Fe$_3$O$_4$ in the reused catalyst after six times reuse, confirming that the structure of the catalyst did not considerably change during the photocatalysis process. In addition, the FTIR spectra of the reused N-MgO@Fe$_3$O$_4$ material was also observed (Fig. S10b), indicating that the main surface functional groups of the as-prepared material were almost fully preserved during the reuse tests. In addition, comparing the TEM images of the catalyst before and after reuse (Fig. S10c) we see that there is no considerable change in the morphology of the N-MgO@Fe$_3$O$_4$ after being used as catalyst in the developed process.

XPS analysis was also applied to further evaluate the reusability capacity of N-MgO@Fe$_3$O$_4$ before and after IMD degradation (Fig. 2d, f, h). Based on the results, all the binding energies including Mg 2p, O 1 s, N 1 s, and Fe 2p orbitals were relatively close to the fresh catalyst, further confirming the structural impeccability of the reused N-MgO@Fe$_3$O$_4$.

To investigate the stability of as-made N-MgO@Fe$_3$O$_4$ material, the

Fig. 9. Matrix effects, reusability and IMD decomposition. A) Effect of water matrix on IMD degradation in the N-MgO@Fe$_3$O$_4$/VL/PMS process (IMD=10 mg/L, PMS=75 mg/L, anion=1 mM, starting pH=5.6, time=60 min; tap water: TDS=303 mg/L, pH=7.2). B) Recyclability of N-MgO@Fe$_3$O$_4$ in the developed catalytic VL/PMS process (IMD=10 mg/L, pH=5.6, PMS=75 mg/L, time=60 min). C) The degradation, mineralization, dechlorination and denitrogenation of IMD in the N-MgO@Fe$_3$O$_4$/VL/PMS process (IMD=10 mg/L, PMS=75 mg/L, pH=5.6).

amount of iron and magnesium leached to the solution was measured during the repetitive cycles by ICP analysis. The findings (Table S1) summarize the significant Fe and Mg leached from the catalyst into the solution during six repetitive reusing cycles of the as-made catalyst. These results showed that the as-made catalyst is stable and durable [89]. In addition, the low concentration of Fe and Mg in the solution during the reuse cycles implies that the contribution of the leached ions in generating homogeneous IMD degradation reactions was negligible.

3.3.3. Insights on IMD decomposition: denitrogenation/dechlorination, mineralization, and reaction intermediates towards its elimination

Along with IMD degradation, the mineralization of IMD during the photocatalytic process was measured by TOC analysis. Accordingly, TOC removal was observed at about 47.5, 63.8, 79, and 91% for 30-, 60-, 90-, and 120-min reaction times, respectively (Fig. 9c). As expected, the synergistic effect between the as-made catalyst/light and PMS played a significant role in mineralization at a later stage time compared to IMD removal due to resistant rings and molecules. Besides, the electron-hole pairs can be generated and then by activation of PMS, lead to IMD mineralization to inorganic compounds (Eq. 32).

$$C_9H_{10}O_2N_5Cl + 17.5O_2 \xrightarrow{\text{Catalyst/VL/PMS}} 9CO_2 + 5HNO_3 + 2H_2O + HCl$$

(32)
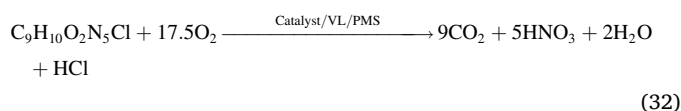
According to Table 1, Tan et al. [7] obtained 41.6% TOC elimination for the concentration of 3 mg/L IMD under visible light process at 120 min. In another study conducted by Zabar et al. [66] TOC removal was 19.1% in the TiO$_2$/UVA process operated at IMD of 100 mg/L, pH of 7, and time of 120 min. In the present study, a high degree of TOC removal at 120 min can demonstrate that the IMD molecules were effectively broken down into smaller intermediates.

In addition, dechlorination and denitrogenation of IMD were investigated in the photocatalytic/PMS process under optimum conditions and the results are depicted in Fig. 9c. It is seen that the dechlorination almost corresponded to the degradation of IMD and over 99% of dechlorination was observed at the reaction time of 90 min. This can be related to the low energy bond of C-Cl (Table S2), which was easily cleaved, and chloride was released into the solution. Nearly complete dechlorination of IMD in the TiO$_2$/UVA process after 120 min has been reported by Kitsiou et al. [71]. However, based on Fig. 9c, the rate of denitrogenation in the reaction time below 60 min was low due to the high energy bond of C-N and particularly C=N bonds, and to the low oxidation state of nitrogen in IMD [66]. Nonetheless, it improved by extending the reaction time and reached around 90% in 120 min where 91% of IMD was mineralized, due mainly to increased formation of reactive degrading species. The denitrogenation being so similar to the mineralization suggests that most of the nitrogen-containing bonds resisted degradation and resulted in the conversion of nitrogen in IMD molecules to inorganic nitrogen species. The efficacy of IMD mineralization and denitrogenation was 90% and 50%, respectively, in the TiO$_2$/UVA/Fe^{3+}/H$_2$O$_2$ process [71].

Finally, for a deeper understanding of the pathways, which lead to IMD degradation, the intermediates' identification was conducted by LC-MS spectra under optimum conditions at 120 min (Fig. 10). Pure IMD solution was injected before irradiation which indicated peaks at a retention time of 2.24 min with $m/z = 256$. Based on the observed peaks, eight different intermediates were identified from IMD degradation, including Imidacloprid urea ($m/z = 212$), Imidacloprid desnitro-olefine ($m/z = 209$), Imidacloprid guanidine ($m/z = 238$), 6-chloronicotinic aldehyde ($m/z = 141$), 2-chloro-5-methylpyridine ($m/z = 115$), Pyridine ($m/z = 71.5$), Guanidine ($m/z = 41.5$), 1-Buten ($m/z = 49$).

The main intermediates identified during the degradation of IMD in the developed process are given in Table 2. Accordingly, two different pathways proposed for IMD decomposition are shown in Fig. 10. IMD molecules can be degraded to product P1 under visible light that is
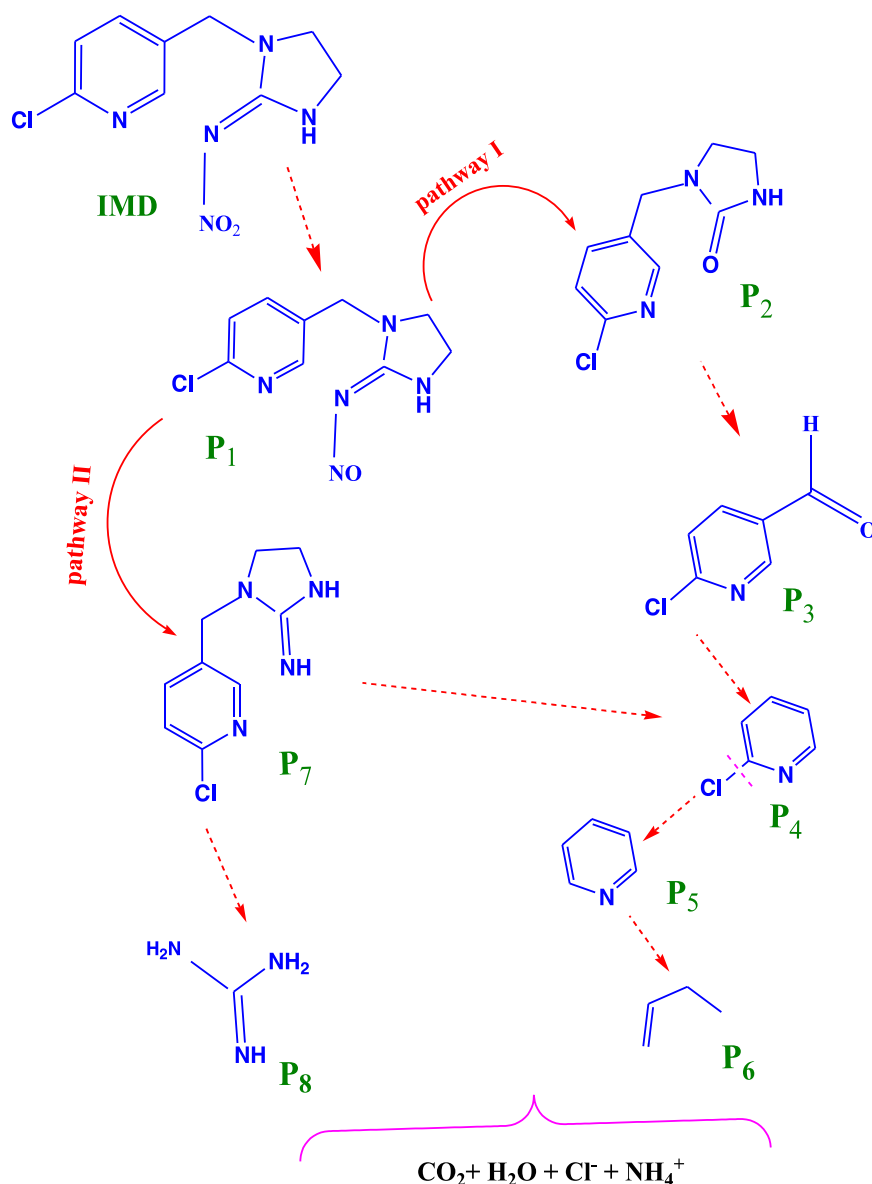
Fig. 10. Proposed pathway for IMD decomposition in the N-MgO@Fe$_3$O$_4$/VL/PMS process (IMD=10 mg/L, pH=5.6, PMS=75 mg/L, time=120 min).

decomposed to product P2 and P3 via attack of ROS. It should be noted that the presence of product P3 in pathway I revealed that IMD mineralization has been successful. It is a non-toxic compound and easily degrades into a simple product. Following the degradation trend, demethylation of product P4 can be transformed to product P5, which is finally transformed into product P6 during the dechlorination. Continuing the oxidation reactions of IMD intermediates with the generated reactive species caused the decomposition of benzene rings with cleavage of N-C and N-N bonds and the formation of products P7 and P8. The intermediates formed in both pathways are finally converted to H$_2$O, CO$_2$, Cl$^-$ and NH$_4^+$ mineral products. As a result, since the N-C bond has almost the lowest energy compared to the other bonds in the structure of the IMD molecule (Table S2), the degradation of IMD could mainly begin with the cleavage of the N-C bond between the pyridine and imidazolidine rings by the oxidative species formed in the reaction [90–92]. Prolonging the reaction could lead to the further breaking down of the intermediates into CO$_2$, NO$_3^-$, and Cl$^-$ [90].
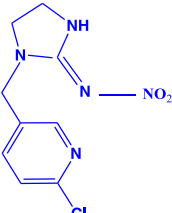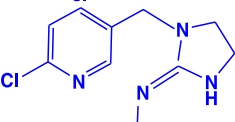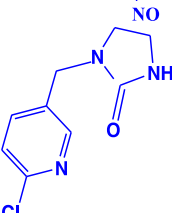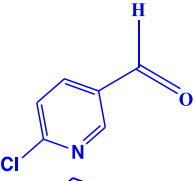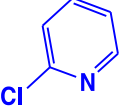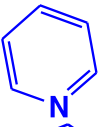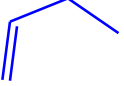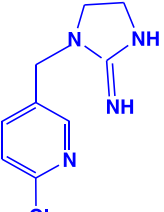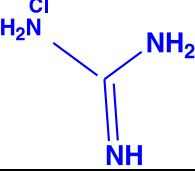
3.4. Bacterial inactivation of the N-MgO@Fe$_3$O$_4$/VL/PMS process: analogies and differences with IMD, and IMD presence effects on disinfection

To expand the investigation on the catalytic capacity of the developed process, the inactivation of a gram-Negative and a gram-Positive bacterial strain was assessed. The kinetics are contrasted with experiments including IMD presence and/or with the different experimental conditions selected, all under visible light (the tests presented are all under VL since dark adsorption had a negligible effect and VL at this wavelength did not lead to PMS activation, and the applied wavelength/intensity did not exert bacterial inactivation [100,101]; hence these data are not shown); the results are presented in Fig. (11 a-c).

The main difference in the presented disinfection tests compared to IMD degradation is that the dominant pathways have mildly altered effects (Fig. 11a). PMS is effectively inactivating *E. coli*, due to its direct effects on the cell [93,94], as previously seen in literature [11,42]. IMD degradation was only mildly affected by PMS (slightly over 20% in a 60 min reaction time) while PMS in 10 min was found to inflict total inactivation. Interestingly, although IMD degradation is low by PMS, the by-products of degradation were toxic for *E. coli* and acted

Table 2
The degradation intermediates identified during the degradation of IMD in the developed process.

(By)product	Experimental m/z	Best possible chemical formula	Structure	Adduct	Reaction time (min)
IMD	256	$C_9H_{10}ClN_5O_2$		[M+H]	2.24
P1	238	$C_9H_{10}ClN_5O$		[M+H]	2.17
P2	212	$C_9H_{10}ClN_3O$		[M+H]	2.18
P3	141	C_6H_4ClNO		[M+H]	1.29
P4	113	C_5H_4ClN		[M+H]	1.18
P5	71.5	C_5H_5N		[2 M+ACN+Na]	3.04
P6	49	C_4H_8		[2 M+CAN+H]	4.29
P7	209	$C_9H_{11}ClN_4$		[M+H]	2.15
P8	59	CH_5N_3		[2 M+Na]	4.30

synergistically; the time for total bacterial inactivation was halved. We note that this effect is clearly deriving from the IMD by-products, as the parent compound (IMD itself), did not have a toxic/inhibitory effect on bacteria over the reaction time (and extended to longer times; see Fig. S11).

When N-MgO@Fe$_3$O$_4$ (denoted as Cat.) was introduced into the system (Fig. 11b) the pathways were altered anew. The time necessary for total inactivation was slightly longer than in its absence. This could

be an indication of a change in the reactive species that dominate inactivation, as well as the localization of the damage:

i) PMS alone will surely react with the cellular membrane, but its possible intracellular action is yet to be determined;
ii) The addition of the catalysts enhances the radical generation in the bulk instead of the intracellular domain, which may be less germicidal since key intracellular targets may no longer be hit and
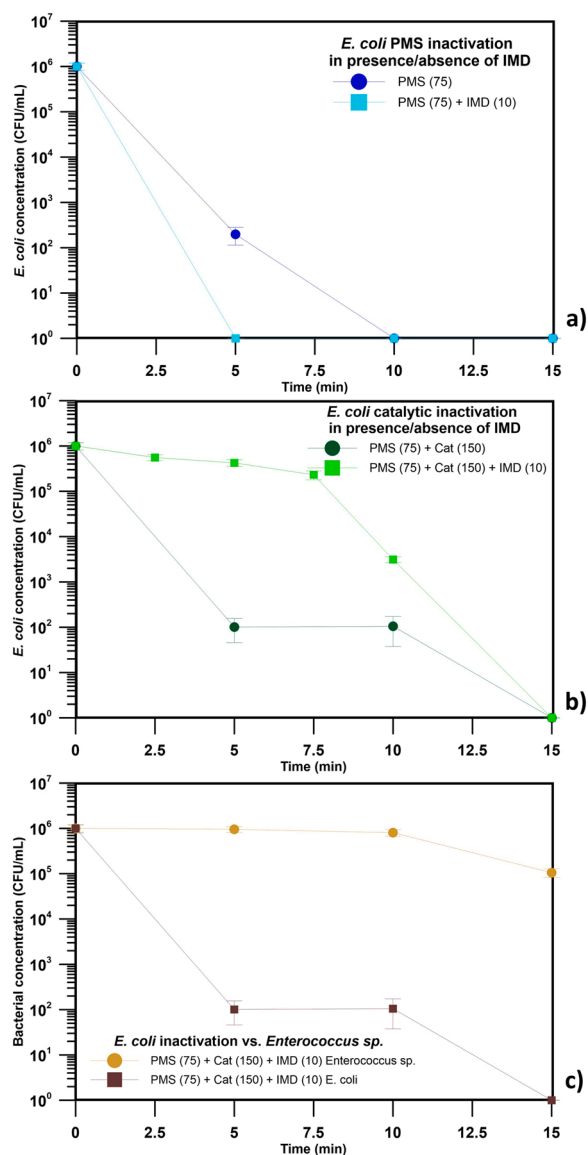
Fig. 11. Inactivation of bacteria via the developed N-MgO@Fe₃O₄/VL/PMS system. A) VL/PMS-induced inactivation of *E. coli* in absence of the catalyst. B) Photocatalytic N-MgO@Fe₃O₄/VL/PMS inactivation of *E. coli*. C) Comparison of the photocatalytic N-MgO@Fe₃O₄/VL/PMS inactivation of *E. coli* vs. *Enterococcus sp*.

inactivation may relie on the extracellular process, i.e. the rupture of the membrane by sequential PPRI attacks.

Given the above considerations, it cannot be excluded that PMS is acting intracellularly or a more complex mechanism is present, as has been recently postulated [102].

Moreover, the addition of IMD in the bulk considerably delays bacterial inactivation. The first phase of inactivation is characterized by a lag, which is an effect of the distribution of the same amounts of active species to more targets, as well as the higher rates of reaction with IMD rather than *E. coli* (HO• and SO₄•⁻ react with IMD with rate constants of $2.7\text{--}3.8 \times 10^9$ M⁻¹ s⁻¹ [59], and $3 \pm 1 \times 10^8$ M⁻¹s⁻¹, respectively [58], while for *E. coli* is 2.8×10^8 M⁻¹ s⁻¹ and $1.39 \pm 0.1 \times 10^9$ M⁻¹ s⁻¹) [95, 96]; this probably means that HO• is surely produced in the system, driving an exogenous inactivation [97]. Hence, in a possible co-existence of targets, such as wastewaters, a delay in inactivation will occur, but is not expected to importantly overpass the time envisioned.

Finally, the inactivation of *Enterococcus sp.* was compared with the

respective of *E. coli* under the N-MgO@Fe₃O₄/VL/PMS system (Fig. 11c). Within the studied time (15 min) only 1 log inactivation of *Enterococcus sp.* was attained, vs. the total inactivation of *E. coli*. Taking into account that *E. faecalis* (of the same bacterial family) has a second-order reaction rate with SO₄•⁻ of $6.71 \pm 0.1 \times 10^9$ M⁻¹ s⁻¹ [96,98], which is x5 times higher than the respective for *E. coli* [95,99], this may imply a HO•-dominated degradation mechanism, and that the gram-Positive cell-wall components (possibly peptidoglycan) confer higher resistance to extracellular oxidation mechanisms.

In summary, bacterial inactivation was more notable and rapid, compared to IMD, and was possible even in the presence of competitive IMD concentration levels. As such, the application of the N-MgO@-Fe₃O₄/VL/PMS system could be an option for the simultaneous disinfection and decontamination of effluents. Nevertheless, besides the evaluation of our developed photocatalytic process, the results of *Enterococcus sp.* compared to *E. coli* stress the necessity to expand the targets when studying the disinfection of aqueous matrices.

4. Conclusions

In this study, N-MgO@Fe₃O₄ nanosheets were successfully synthesized by a sol-gel method as a novel photocatalyst for IMD degradation by PMS activation under light. The N-MgO@Fe₃O₄/VL/PMS process indicated high IMD degradation and mineralization rates under optimum conditions, which involve very low catalyst and PMS concentrations. This feature renders the system relatively economic, considering the available photocatalytic materials in literature. Furthermore, assessing the stepwise construction of the catalyst, the synergies among the different components, and the catalyst and visible light and PMS, lead to high synergy and ultimately a high reaction rate, compared to the existing published studies.

In addition to investigating the common parameters (PMS dosages, catalyst concentration, solution pH, reaction time), the effect of scavengers and water matrix were also checked on the trend of IMD removal under the photocatalytic/PMS process. The order of negative effect of water matrix on IMD degradation was HCO₃⁻ >PO₄³⁻ >NO₃⁻ >Cl⁻; only the first two could completely block the process, albeit in very high concentrations, while experiments in tap water presented insignificant differences, which allow consideration for further use in natural waters.

Scavenger experiments and EPR analysis revealed that HO•, SO₄•⁻ and ¹O₂ are generated and all three reactive species play significant role in the IMD degradation mechanism exerted by the N-MgO@Fe₃O₄/VL/PMS process. These allowed the elucidation and description of the basic decomposition mechanisms and the suggestion of the IMD degradation pathway towards its complete mineralization. Besides, based on the results of XPS, XRD, TEM and ICP after reaction, the introduced catalyst showed that it has high reusability and stability. Insignificant leaching was measured, while for at least 5 re-use cylces, the efficacy of the reaction remained well above the 80% found by the pristine catalyst.

Finally, the experiments in presence of bacteria showed that compared to IMD, *E. coli* are expected to be eliminated much faster. They also revealed the possible implications of IMD transformation (intermediates, dechlorination by-products) which enhanced bacterial killing. However, the above considerations were not validated against *Enterococcus sp.*, which indicates the need for a larger battery of disinfection tests necessary, to confirm proper disinfection. Nevertheless, the first results demonstrate the high efficacy of the composite catalyst and permit considerations for further use in environmental remediation applications.

CRediT authorship contribution statement

Somaye Akbari: Investigation, Formal analysis, Writing – original draft, Writing – review & editing, Visualization. **Gholamreza Moussavi**: Conceptualization, Methodology, Resources, Writing – original

draft, Writing – review & editing, Supervision, Project administration, Funding acquisition. **Jeremie Decker**: Investigation, Validation, Writing – review & editing. **Maria Luisa Marin**: Investigation, Writing – original draft, Writing – review & editing, Visualization. **Francisco Bosca**: Investigation, Writing – original draft, Writing – review & editing, Visualization. **Stefanos Giannakis**: Resources, Writing – original draft, Writing – review & editing, Supervision, Visualization, Project administration.

Declaration of Competing Interest

The authors declare that they have no known competing financial interests or personal relationships that could have appeared to influence the work reported in this paper.

Data Availability

Data will be made available on request.

Appendix A. Supporting information

Supplementary data associated with this article can be found in the online version at doi:10.1016/j.apcatb.2022.121732.

References

[1] P.V.L. Reddy, K.H. Kim, A review of photochemical approaches for the treatment of a wide range of pesticides, J. Hazard Mater. 285 (2015) 325–335.

[2] C. Li, Y. Huang, X. Dong, Z. Sun, X. Duan, B. Ren, et al., Highly efficient activation of peroxymonosulfate by natural negatively-charged kaolinite with abundant hydroxyl groups for the degradation of atrazine, Appl. Catal. B 247 (2019) 10–23.

[3] X. Liu, X. Wu, Z. Long, C. Zhang, Y. Ma, X. Hao, et al., Photodegradation of imidacloprid in aqueous solution by the metal-free catalyst graphitic carbon nitride using an energy-saving lamp, J. Agric. Food Chem. 63 (2015) 4754–4760.

[4] O. Iglesias, J. Gomez, M. Pazos, M.A. Sanroman, Electro-Fenton oxidation of imidacloprid by Fe alginate gel beads, Appl. Catal. B 144 (2014) 416–424.

[5] P. Soriano-Molina, S. Miralles-Cuevas, I. Oller, J.G. Sanchez, J.S. Perez, Contribution of temperature and photon absorption on solar photo-Fenton mediated by Fe^{3+}-NTA for CEC removal in municipal wastewater, Appl. Catal. B 294 (2021) 120251.

[6] P. Meng, H. Heng, Y. Sun, X. Liu, In situ polymerization synthesis of Z-scheme tungsten trioxide/polyimide photocatalyst with enhanced visible-light photocatalytic activity, Appl. Surf. Sci. 428 (2018) 1130–1140.

[7] J. Tan, Z. Li, J. Li, Y. Meng, X. Yao, Y. Wang, et al., Visible-light-assisted peroxymonosulfate activation by metal-free bifunctional oxygen-doped graphitic carbon nitride for enhanced degradation of imidacloprid: role of non-photochemical and photocatalytic activation pathway, J. Hazard Mater. 423 (2022), 127048.

[8] Z. Amiri, G. Moussavi, S. Mohammadi, S. Giannakis, Development of a VUV-UVC/peroxymonosulfate, continuous-flow Advanced Oxidation Process for surface water disinfection and Natural Organic Matter elimination: application and mechanistic aspects, J. Hazard Mater. 408 (2021), 124634.

[9] M.R. Vucic, R. Baosic, J. Mitrovic, M. Petrovic, N. Velinov, M. Kostic, et al., Comparison of the advanced oxidation processes in the degradation of pharmaceuticals and pesticides in simulated urban wastewater: principal component analysis and energy requirements, Process Saf. Environ. Prot. 149 (2021) 786–793.

[10] L. Zhou, X. Zhang, M. Cai, N. Cui, G. Chen, G. Zou, New insights into the efficient charge transfer of the modified-TiO_2/Ag_3PO_4 composite for enhanced photocatalytic destruction of algal cells under visible light, Appl. Catal. B 302 (2022), 120868.

[11] M. Kohantorabi, S. Giannakis, G. Moussavi, M. Bensimon, M.R. Gholami, C. Pulgarin, An innovative, highly stable Ag/ZIF-67@GO nanocomposite with exceptional peroxymonosulfate (PMS) activation efficacy, for the destruction of chemical and microbiological contaminants under visible light, J. Hazard Mater. 413 (2021), 125308.

[12] Q. Ji, X. Cheng, Y. Wu, W. Xiang, H. He, Z. Xu Z, et al., Visible light absorption by perylene diimide for synergistic persulfate activation towards efficient photodegradation of bisphenol A, Appl. Catal. B 282 (2021), 119579.

[13] J. Wang, C.S. Cao, J. Wang, Y. Zhang, L. Zhu, Insights into highly efficient photodegradation of poly/perfluoroalkyl substances by In-MOF/BiOF heterojunctions: built-in electric field and strong urface adsorption, Appl. Catal. B 304 (2022), 121013.

[14] Z. Rao, G. Lu, A. Mahmood, G. Shi, X. Xie, J. Sun, Deactivation and activation mechanism of TiO_2 and rGO/Er^{3+}-TiO_2 during flowing gaseous VOCs photodegradation, Appl. Catal. B 284 (2021), 119813.

[15] M. Moradi, F. Hasanvandian, A.A. Isari, F. Hayati, B. Kakavandi, S.R. Setayesh, CuO and ZnO co-anchored on g-C_3N_4 nanosheets as an affordable double Z-scheme nanocomposite for photocatalytic decontamination of amoxicillin, Appl. Catal. B 285 (2021), 119838.

[16] M. Wang, G. Tan, D. Zhang, B. Li, L. Lv, Y. Wang, et al., Defect-mediated Z-scheme BiO_2-x/Bi_2O_2. 75 photocatalyst for full spectrum solar-driven organic dyes degradation, Appl. Catal. B 254 (2019) 98–112.

[17] S. Li, Q. Wang, X. Yan, H.Q. Zhuang, C. Yuan, J. Feng, et al., Al_2O_3 support triggering highly efficient photoreduction of CO_2 with H_2O on noble-metal-free $CdS/Ni9S8/Al_2O_3$, Appl. Catal. B 240 (2019) 174–181.

[18] Z.W. Heng, W.C. Chong, Y.L. Pang, C.H. Koo, An overview of the recent advances of carbon quantum dots/metal oxides in the application of heterogeneous photocatalysis in photodegradation of pollutants towards visible-light and solar energy exploitation, J. Environ. Chem. Eng. 9 (2021), 105199.

[19] F. Fanaei, G. Moussavi, V. Srivastava, M. Sillanpaa, The enhanced catalytic potential of sulfur-doped MgO (S-MgO) nanoparticles in activation of peroxysulfates for advanced oxidation of acetaminophen, Chem. Eng. J. 371 (2019) 404–413.

[20] G. Moussavi, A. Khavanin, R. Alizadeh, The integration of ozonation catalyzed with MgO nanocrystals and the biodegradation for the removal of phenol from saline wastewater, Appl. Catal. B 97 (2010) 160–167.

[21] S. Akbari, G. Moussavi, S. Giannakis, Efficient photocatalytic degradation of ciprofloxacin under UVA-LED, using S, N-doped MgO nanoparticles: synthesis, parametrization and mechanistic interpretation, J. Mol. Liq. 324 (2021) 114831.

[22] A. Zhang, H. Ai, M.L. Fu, Y.B. Hu, J. Liu, Y. Ji, et al., A new insight into catalytic ozonation of ammonia by MgO/Co_3O_4 composite: The effects, reaction kinetics and mechanism, Chem. Eng. J. 418 (2021), 129461.

[23] C. Yang, Y. Wang, H. Fan, G. de Falco, S. Yang, J. Shangguan, et al., Bifunctional ZnO-MgO/activated carbon adsorbents boost H_2S room temperature adsorption and catalytic oxidation, Appl. Catal. B 266 (2020), 118674.

[24] B. Nguegang, V. Masindi, T.A.M. Makudali, M. Tekere, Effective treatment of acid mine drainage using a combination of MgO-nanoparticles and a series of constructed wetlands planted with Vetiveria zizanioides: a hybrid and stepwise approach, J. Environ. Manag 310 (2022), 114751.

[25] L. Pan, T. Muhammad, L. Ma, Z.F. Huang, S. Wang, L. Wang, et al., MOF-derived C-doped ZnO prepared via a two-step calcination for efficient photocatalysis, Appl. Catal. B 189 (2016) 181–191.

[26] D. Li, C. Wen, J. Huang, J. Zhong, P. Chen, H. Liu, et al., High-efficiency ultrathin porous phosphorus-doped graphitic carbon nitride nanosheet photocatalyst for energy production and environmental remediation, Appl. Catal. B (2022), 121099.

[27] M. Bindhu, T.D. Willington, M.R. Hatshan, S.M. Chen, T.W. Chen, Environmental photochemistry with Sn/F simultaneously doped TiO_2 nanoparticles: UV and visible light induced degradation of thiazine dye, Environ. Res 207 (2022), 112108.

[28] W. Wang, M.O. Tade, Z. Shao, Nitrogen-doped simple and complex oxides for photocatalysis: a review, Prog. Mater. Sci. 92 (2018) 33–63.

[29] J. Huang, L. Dou, J. Li, J. Zhong, M. Li, T. Wang, Excellent visible light responsive photocatalytic behavior of N-doped TiO_2 toward decontamination of organic pollutants, J. Hazard Mater. 403 (2021), 123857.

[30] L. Sun, Q. Shao, Y. Zhang, H. Jiang, S. Ge, S. Lou, et al., N self-doped ZnO derived from microwave hydrothermal synthesized zeolitic imidazolate framework-8 toward enhanced photocatalytic degradation of methylene blue, J. Colloid Interface Sci. 565 (2020) 142–155.

[31] M. Kohantorabi, G. Moussavi, P. Oulego, S. Giannakis, Radical-based degradation of sulfamethoxazole via UVA/PMS-assisted photocatalysis, driven by magnetically separable Fe_3O_4@ CeO_2@BiOI nanospheres, Sep Purif. Technol. 267 (2021), 118665.

[32] A.H. Cheshme Khavar, G. Moussavi, A. Mahjoub, K. Yaghmaeian, V. Srivastava, M. Sillanpaa, et al., Novel magnetic Fe_3O_4@rGO@ZnO onion-like microspheres decorated with Ag nanoparticles for the efficient photocatalytic oxidation of metformin: toxicity evaluation and insights into the mechanisms, Catal. Sci. Technol. 9 (2019) 5819–5837.

[33] X. Xie, S. Li, K. Qi, Z. Wang, Photoinduced synthesis of green photocatalyst Fe_3O_4/BiOBr/CQDs derived from corncob biomass for carbamazepine degradation: the role of selectively more CQDs decoration and Z-scheme structure, Chem. Eng. J. 420 (2021), 129705.

[34] F. Ghanbari, J. Wu, M. Khatebasreh, D. Ding, K.Y.A. Lin, Efficient treatment for landfill leachate through sequential electrocoagulation, electrooxidation and PMS/UV/CuFe$_2$O$_4$ process, Sep Purif. Technol. 242 (2020), 116828.

[35] X. Liu, J. Wang, D. Wu, Z. Wang, Y. Li, X. Fan, et al., N-doped carbon dots decorated 3D g-C$_3$N$_4$ for visible-light driven peroxydisulfate activation: insights of non-radical route induced by Na$^+$ doping, Appl. Catal. B 310 (2022), 121304.

[36] S. Akbari, F. Ghanbari, M. Moradi, Bisphenol A degradation in aqueous solutions by electrogenerated ferrous ion activated ozone, hydrogen peroxide and persulfate: applying low current density for oxidation mechanism, Chem. Eng. J. 294 (2016) 298–307.

[37] M. Kohantorabi, G. Moussavi, S. Giannakis, A review of the innovations in metal- and carbon-based catalysts explored for heterogeneous peroxymonosulfate (PMS) activation, with focus on radical vs. non-radical degradation pathways of organic contaminants, Chem. Eng. J. (2020), 127957.

[38] S. Varjani, A. Pandey, R. Tyagi, N.H. Ngo, C. Larroche, Constructed wetlands for the removal of organic micro-pollutants, in: Sunita Varjani, Ashok Pandey, R. D. Tyagi, Huu Hao Ngo, Christian Larroche (Eds.), Current Developments in Biotechnology and Bioengineering: Emerging Organic Micro-Pollutants, Elsevier, 2020, pp. 87–140.

[39] Y. Xu, X. Shi, R. Hua, R. Zhang, Y. Yao, B. Zhao, et al., Remarkably catalytic activity in reduction of 4-nitrophenol and methylene blue by Fe$_3$O$_4$@COF supported noble metal nanoparticles, Appl. Catal. B 260 (2020), 118142.

[40] Q. Si, Q. Wen, Q. Yang, Y. Song, Y. Li, Preparation of β-cyclodextrin/Fe$_3$O$_4$/polyvinylpyrrolidone composite magnetic microspheres for the adsorption of methyl orange, Chem. Res Chin. Univ. 33 (2017) 1012–1016.

[41] G. Gai, L. Wang, X. Dong, S. Xu, Electrospun Fe$_3$O$_4$/PVP//Tb (BA) 3phen/PVP magnetic–photoluminescent bifunctional bistrand aligned composite nanofibers bundles, J. Mater. Sci. 48 (2013) 5140–5147.

[42] S. Mohammadi, G. Moussavi, M. Shekoohiyan, M.L. Marin, F. Bosca, S. Giannakis, A continuous-flow catalytic process with natural hematite-alginate beads for effective water decontamination and disinfection: Peroxymonosulfate activation leading to dominant sulfate radical and minor non-radical pathways, Chem. Eng. J. 411 (2021), 127738.

[43] P.O. Diez, S. Giannakis, J. Rodríguez-Chueca, D. Wang, B. Quilty, R. Devery, et al., Enhancing solar disinfection (SODIS) with the photo-Fenton or the Fe^{2+}/peroxymonosulfate-activation process in large-scale plastic bottles leads to toxicologically safe drinking water, Water Res 186 (2020), 116387.

[44] J. Liu, J. Jiang, A. Aihemaiti, Y. Meng, M. Yang, Y. Xu, et al., Removal of phosphate from aqueous solution using MgO-modified magnetic biochar derived from anaerobic digestion residue, J. Environ. Manag 250 (2019), 109438.

[45] B.M. Chong, N.H.N. Azman, M.A.A. Mohd Abdah, Y. Sulaiman, Supercapacitive performance of N-doped graphene/Mn$_3$O$_4$/Fe$_3$O$_4$ as an electrode material, Appl. Sci. 9 (2019) 1040.

[46] F. Bekena, D.H. Kuo, 10 nm sized visible light TiO$_2$ photocatalyst in the presence of MgO for degradation of methylene blue, Mater. Sci. Semicond. Process 116 (2020) 105–152.

[47] Z. Jin, Y. Jia, T. Luo, L.T. Kong, B. Sun, W. Shen, et al., Efficient removal of fluoride by hierarchical MgO microspheres: Performance and mechanism study, Appl. Surf. Sci. 357 (2015) 1080–1088.

[48] X. Zhu, D. Wu, W. Wang, F. Tan, P.K. Wong, X. Wang, et al., Highly effective antibacterial activity and synergistic effect of Ag-MgO nanocomposite against Escherichia coli, J. Alloy. Compd. 684 (2016) 282–290.

[49] M. Kohantorabi, G. Moussavi, S. Mohammadi, P. Oulego, S. Giannakis, Photocatalytic activation of peroxymonosulfate (PMS) by novel mesoporous Ag/ZnO@ NiFe$_2$O$_4$ nanorods, inducing radical-mediated acetaminophen degradation under UVA irradiation, Chemosphere 277 (2021), 130271.

[50] C. Li, J. Wu, W. Peng, Z. Fang, J. Liu, Peroxymonosulfate activation for efficient sulfamethoxazole degradation by Fe$_3$O$_4$/β-FeOOH nanocomposites: coexistence of radical and non-radical reactions, Chem. Eng. J. 356 (2019) 904–914.

[51] C. Tan, N. Gao, Y. Deng, J. Deng, S. Zhou, J. Li, et al., Radical induced degradation of acetaminophen with Fe$_3$O$_4$ magnetic nanoparticles as heterogeneous activator of peroxymonosulfate, J. Hazard Mater. 276 (2014) 452–460.

[52] Q. Wang, Y. Cui, R. Huang, L. Zhong, P. Yan, S. Zhang, et al., A heterogeneous Fenton reaction system of N-doped TiO$_2$ anchored on sepiolite activates peroxymonosulfate under visible light irradiation, Chem. Eng. J. 383 (2020), 123142.

[53] S.S. Kekade, P.V. Gaikwad, S.A. Raut, R.J. Choudhary, V.L. Mathe, D. Phase, et al., Electronic structure of visible light-driven photocatalyst δ-Bi$_{11}$VO$_{19}$ nanoparticles synthesized by thermal plasma, ACS Omega 3 (2018) 5853–5864.

[54] F. Guo, X. Jiang, X. Li, X. Jia, S. Liang, L. Qian, Synthesis of MgO/Fe$_3$O$_4$ nanoparticles embedded activated carbon from biomass for high-efficient adsorption of malachite green, Mater. Chem. Phys. 240 (2020) 122240.

[55] M.S. Akple, J. Low, Z. Qin, S. Wageh, A.A. Al-Ghamdi, J. Yu, et al., Nitrogen-doped TiO$_2$ microsheets with enhanced visible light photocatalytic activity for CO$_2$ reduction, Chin. J. Catal. 36 (2015) 2127–2134.

[56] H. Guo, H.Y. Niu, C. Liang, C.G. Niu, Y. Liu, N. Tang, et al., Few-layer graphitic carbon nitride nanosheet with controllable functionalization as an effective metal-free activator for peroxymonosulfate photocatalytic activation: role of the energy band bending, Chem. Eng. J. 401 (2020), 126072.

[57] K.Y.A. Lin, Z.Y. Zhang, Degradation of Bisphenol A using peroxymonosulfate activated by one-step prepared sulfur-doped carbon nitride as a metal-free heterogeneous catalyst, Chem. Eng. J. 313 (2017) 1320–1327.

[58] R. Guo, Y. Wang, J. Li, X. Cheng, D.D. Dionysiou, Sulfamethoxazole degradation by visible light assisted peroxymonosulfate process based on nanohybrid manganese dioxide incorporating ferric oxide, Appl. Catal. B 278 (2020), 119297.

[59] S. Chen S, J. Deng, Y. Deng, N. Gao, Influencing factors and kinetic studies of imidacloprid degradation by ozonation, Environ. Technol. 40 (2019) 2127–2134.

[60] G. Rozsa G, M. Nafradi, T. Alapi, K. Schrantz, L. Szabo, L. Wojnarovits, et al., Photocatalytic, photolytic and radiolytic elimination of imidacloprid from aqueous solution: reaction mechanism, efficiency and economic considerations, Appl. Catal. B 250 (2019) 429–439.

[61] Q. Wang, P. Rao, G. Li, L. Dong, X. Zhang, Y. Shao, et al., Degradation of imidacloprid by UV-activated persulfate and peroxymonosulfate processes: kinetics, impact of key factors and degradation pathway, Ecotoxicol. Environ. Saf. 187 (2020), 109779.

[62] J.M.D. Dikdim, Y. Gong, G.B. Noumi, J.M. Sieliechi, X. Zhao, N. Ma, et al., Peroxymonosulfate improved photocatalytic degradation of atrazine by activated carbon/graphitic carbon nitride composite under visible light irradiation, Chemosphere 217 (2019) 833–842.

[63] M. Golshan, B. Kakavandi, M. Ahmadi, M. Azizi, Photocatalytic activation of peroxymonosulfate by TiO$_2$ anchored on cupper ferrite (TiO$_2$@CuFe$_2$O$_4$) into 2,4-D degradation: process feasibility, mechanism and pathway, J. Hazard Mater. 359 (2018) 325–337.

[64] Y. Wu, Z. Fang, Y. Shi, H. Chen, Y. Liu, Y. Wang, et al., Activation of peroxymonosulfate by BiOCl@ Fe$_3$O$_4$ catalyst for the degradation of atenolol: kinetics, parameters, products and mechanism, Chemosphere 216 (2019) 248–257.

[65] F. Ghanbari, M. Ahmadi, F. Gohari, Heterogeneous activation of peroxymonosulfate via nanocomposite CeO$_2$-Fe$_3$O$_4$ for organic pollutants removal: the effect of UV and US irradiation and application for real wastewater, Sep Purif. Technol. 228 (2019), 115732.

[66] R. Zabar, T. Komel, J. Fabjan, M.B. Kralj, P. Trebse, Photocatalytic degradation with immobilised TiO$_2$ of three selected neonicotinoid insecticides: imidacloprid, thiamethoxam and clothianidin, Chemosphere 89 (2012) 293–301.

[67] J. Tang, X. Huang, X. Huang, L. Xiang, Q. Wang, Photocatalytic degradation of imidacloprid in aqueous suspension of TiO$_2$ supported on H-ZSM-5, Environ. Earth Sci. 66 (2012) 441–445.

[68] K. Babic, V. Tomasic, V. Gilja, J. Cunff, V. Gomzi, A. Pintar, et al., Photocatalytic degradation of imidacloprid in the flat-plate photoreactor under UVA and simulated solar irradiance conditions—the influence of operating parameters, kinetics and degradation pathway, J. Environ. Chem. Eng. 9 (2021), 105611.

[69] H. Heng, Q. Gan, P. Meng, X. Liu, H$_3$PW$_{12}$O$_{40}$/TiO$_2$–In$_2$O$_3$: a visible light driven type-II heterojunction photocatalyst for the photocatalytic degradation of imidacloprid, RSC Adv. 6 (2016) 73301–73307.

[70] F. Changgen, X. Gang, L. Xia, Photocatalytic degradation of imidacloprid by composite catalysts H$_3$PW$_{12}$O$_{40}$/La-TiO$_2$, J. Rare Earths 31 (2013) 44–48.

[71] V. Kitsiou, N. Filippidis, D. Mantzavinos, I. Poulios, Heterogeneous and homogeneous photocatalytic degradation of the insecticide imidacloprid in aqueous solutions, Appl. Catal. B Environ. 86 (2009) 27–35.

[72] M. Zangiabadi, A. Saljooqi, T. Shamspur, A. Mostafavi, Evaluation of GO nanosheets decorated by CuFe$_2$O$_4$ and CdS nanoparticles as photocatalyst for the degradation of dinoseb and imidacloprid pesticides, Ceram. Int 46 (2020) 6124–6128.

[73] D. Mohanta, M. Ahmaruzzaman, Au–SnO$_2$–CdS ternary nanoheterojunction composite for enhanced visible light-induced photodegradation of imidacloprid, Environ. Res 201 (2021), 111586.

[74] C. Wu, Facile one-step synthesis of N-doped ZnO micropolyhedrons for efficient photocatalytic degradation of formaldehyde under visible-light irradiation, Appl. Surf. Sci. 319 (2014) 237–243.

[75] Y. Zhao, G. Wang, L. Li, X. Dong, X. Zhang, Enhanced activation of peroxymonosulfate by nitrogen-doped graphene/TiO$_2$ under photo-assistance for organic pollutants degradation: insight into N doping mechanism, Chemosphere 244 (2020), 125526.

[76] G. Nardi, I. Manet, S. Monti, M.A. Miranda, V. Lhiaubet-Vallet, Scope and limitations of the TEMPO/EPR method for singlet oxygen detection: the misleading role of electron transfer, Free Radic. Biol. Med 77 (2014) 64–70.

[77] E. Albiter, S. Alfaro, M.A. Valenzuela, Photosensitized oxidation of 9, 10-dime-thylanthracene with singlet oxygen by using a safranin O/silica composite under visible light, Photochem. Photobio. Sci. 14 (3) (2015) 597–602.

[78] W.D. Oh, Z. Dong, T.T. Lim, Generation of sulfate radical through heterogeneous catalysis for organic contaminants removal: current development, challenges and prospects, Appl. Catal. B Environ. 194 (2016) 169–201.

[79] J.C. Barreto, G.S. Smith, N.H. Strobel, P.A. McQuillin, T.A. Miller, Terephthalic acid: a dosimeter for the detection of hydroxyl radicals in vitro, Life Sci. 56 (1994) 89–96.

[80] J.T. Schneider, D.S. Firak, R.R. Ribeiro, P. Peralta-Zamora, Use of scavenger agents in heterogeneous photocatalysis: truths, half-truths, and misinterpretations, Phys. Chem. Chem. Phys. 22 (2020) 15723–15733.

[81] P. Sun, H. Liu, M. Feng, L. Guo, Z. Zhai, Y. Fang, et al., Nitrogen-sulfur co-doped industrial graphene as an efficient peroxymonosulfate activator: singlet oxygen-dominated catalytic degradation of organic contaminants, Appl. Catal. B 251 (2019) 335–345.

[82] Q. Kan, K. Lu, S. Dong, D. Shen, Q. Huang, Y. Tong, et al., Transformation and removal of imidacloprid mediated by silver ferrite nanoparticle facilitated peroxymonosulfate activation in water: Reaction rates, products, and pathways, Environ. Pollut. 267 (2020), 115438.

[83] J. Huang, H. Zhang, Mn-based catalysts for sulfate radical-based advanced oxidation processes: a review, Environ. Int 105 (2019) 133–141.

[84] J. Criquet, N.K.V. Leitner, Reaction pathway of the degradation of the p-hydroxybenzoic acid by sulfate radical generated by ionizing radiations, Radiat. Phys. Chem. 106 (2015) 307–314.

[85] P. Duan, T. Ma, Y. Yue, Y. Li, X. Zhang, Y. Shang, et al., Fe/Mn nanoparticles encapsulated in nitrogen-doped carbon nanotubes as a peroxymonosulfate activator for acetamiprid degradation, Environ. Sci. Nano 6 (2019) 1799–17811.

[86] Z. Chen, L. Wang, H. Xu, Q. Wen, Efficient heterogeneous activation of peroxymonosulfate by modified $CuFe_2O_4$ for degradation of tetrabromobisphenol A, Chem. Eng. J. 389 (2020), 124345.

[87] X. Cui, X. Liu, C. Lin, M. He, W. Ouyang, Activation of peroxymonosulfate using drinking water treatment residuals modified by hydrothermal treatment for imidacloprid degradation, Chemosphere 254 (2020), 126820.

[88] Y. Wang, X. Zhao, D. Cao, Y. Wang, Y. Zhu, Peroxymonosulfate enhanced visible light photocatalytic degradation bisphenol A by single-atom dispersed Ag mesoporous $g-C_3N_4$ hybrid, Appl. Catal. B 211 (2017) 79–88.

[89] J. He, P. Lyu, B. Jiang, S. Chang, H. Du, J. Zhu, et al., A novel amorphous alloy photocatalyst (NiB/In_2O_3) composite for sunlight-induced CO_2 hydrogenation to HCOOH, Appl. Catal. B 298 (2021), 120603.

[90] C. Zhang, F. Li, H. Zhang, R. Wen, X. Yi, Y. Yang, et al., Crucial roles of $3D–MoO_2–PBC$ cocatalytic electrodes in the enhanced degradation of imidacloprid in heterogeneous electro–Fenton system: Degradation mechanisms and toxicity attenuation, J. Hazard Mater. 420 (2021), 126556.

[91] S. Karimian S, G. Moussavi, F. Fanaei, S. Mohammadi, S. Shekoohiyan, S. Giannakis, Shedding light on the catalytic synergies between Fe (II) and PMS in vacuum UV (VUV/Fe/PMS) photoreactors for accelerated elimination of pharmaceuticals: the case of metformin, Chem. Eng. J. 400 (2020), 125896.

[92] X. Xu, Z. Ran, G. Wen, Z. Liang, Q. Wan, Z. Chen, et al., Efficient inactivation of bacteria in ballast water by adding potassium peroxymonosulfate alone: Role of halide ions, Chemosphere 253 (2020), 126656.

[93] I. Berruti, I. Oller, M.I. Polo-Lopez, Direct oxidation of peroxymonosulfate under natural solar radiation: accelerating the simultaneous removal of organic contaminants and pathogens from water, Chemosphere 279 (2021), 130555.

[94] R. Xiao, K. Liu, L. Bai, D. Minakata, Y. Seo, R.K. Goktas, et al., Inactivation of pathogenic microorganisms by sulfate radical: present and future, Chem. Eng. J. 371 (2019) 222–232.

[95] R. Xiao, L. Bai, K. Liu, Y. Shi, D. Minakata, C.H. Huang, et al., Elucidating sulfate radical-mediated disinfection profiles and mechanisms of Escherichia coli and Enterococcus faecalis in municipal wastewater, Water Res 173 (2020), 115552.

[96] E.A. Serna-Galvis, J.A. Troyon, S. Giannakis, R.A. Torres-Palma, L. Carena, D. Vione, D, et al., Kinetic modeling of lag times during photo-induced inactivation of E. coli in sunlit surface waters: unraveling the pathways of exogenous action, Water Res 163 (2019), 114894.

[97] Y. Wu, Y. Shi, H. Chen, J. Zhao, W. Dong, Activation of persulfate by magnetite: implications for the degradation of low concentration sulfamethoxazole, Process Saf. Environ. Prot. 116 (2018) 468–476.

[98] G.M. Rodriguez-Muñiz, J. Gomis, A. Arques, A.M. Amat, M.L. Marin, M.A. Miranda, Hydroxyl radical as an unlikely key intermediate in the photodegradation of emerging pollutants, Photochem. Photobiol. 90 (2014) 1467–1469.

[99] S. Giannakis, S. Samoili, J. Rodríguez-Chueca, A meta-analysis of the scientific literature on (photo)Fenton and persulfate advanced oxidation processes: where do we stand and where are we heading to? Curr. Opin. Green Sustain. Chem. 29 (2021), 100456.

[100] Rosa Mosteo, Angelica Varon Lopez, David Muzard, Norberto Benitez, Stefanos Giannakis, Cesar Pulgarin, Visible light plays a significant role during bacterial inactivation by the photo-fenton process, even at sub-critical light intensities, Water Research 174 (2020), 115636, https://doi.org/10.1016/j.watres.2020.115636.

[101] Stefanos Giannakis, Anshika Gupta, Cesar Pulgarin, James Imlay, Identifying the mediators of intracellular E. coli inactivation under UVA light: The (photo) Fenton process and singlet oxygen, Water Research 221 (2022), 118740, https://doi.org/10.1016/j.watres.2022.118740.

[102] Nuria Lopez-Vinent, Alberto Cruz-Alcalde, Gholamreza Moussavi, Isabel del Castillo Gonzalez, Aurelio Hernandez Lehmann, Jaime Gimenez, Stefanos Giannakis, Improving ferrate disinfection and decontamination performance at neutral pH by activating peroxymonosulfate under solar light, Chemical Engineering Journal 450 (Part 1) (2022), 137904, https://doi.org/10.1016/j.cej.2022.137904.